Revision 1

OH-defects in quartz as monitor for igneous, metamorphic and sedimentary processes

Roland Stalder[1*], Alexander Potrafke[1], Kjell Billström[2], Henrik Skogby[2], Guido Meinhold[3], Christian Gögele[1], Thomas Berberich[1]

[1]University Innsbruck, Inst. for Mineralogy and Petrography, Innrain 52f, A-6020 Innsbruck, Austria

[2]Swedish Museum of Natural History, Dept. of Geosciences, S-11418 Stockholm, Sweden

[3]University of Göttingen, Geoscience Center, Goldschmidtstr.3, D-37077 Göttingen, Germany

[*] Corresponding author, e-mail: roland.stalder@uibk.ac.at

Abstract

Oriented sections of more than 500 quartz grains from sediments, igneous and metamorphic rocks from different localities in Sweden, Austria, Germany and South Africa were analyzed by FTIR spectroscopy, and their OH-defect content was determined with respect to the speciation and total defect water content. Systematic variations of defect speciation and statistical evaluation of total defect contents were used to evaluate the potential of FTIR spectroscopy on quartz as a thermometer in quartzite, as a tool for differentiation trends in granitic systems, and for provenance analysis of sedimentary rocks. In addition to the analyses of natural crystals, high-pressure annealing experiments at lower crustal conditions (1-3 kbar and 650-750°C) were performed in order to document the effect of high-grade metamorphism on the defect chemistry. Results indicate that (1) quartz grains from unmetamorphosed granite bodies reveal interesting differentiation trends, (2) sediments and sedimentary rocks are valuable archives to preserve the pre-sedimentary OH-defect chemistry, where individual signatures are preserved and can be traced back to potential source rocks, (3) OH-defects are retained up to 300°C over geological time scales, (4) long-term low-grade metamorphic overprint leads to a continuous annealing to lower defect water contents, where Al-specific OH-defects survive

best, and (5) middle to high-grade annealing drives towards a homogeneous defect partitioning from grain to grain, where the degree of attainment of equilibrium depends on temperature and duration of the thermal event.

In summary, OH-defects in quartz crystals monitor parts of their geological history, and the systematic investigation and statistical treatment of a large amount of grains can be applied as an analytical tool to study sedimentary, metamorphic and igneous processes.

Keywords: quartz, hydrous defects, provenance, quartzite, granite

Introduction

Quartz is an important rock-forming mineral that crystallizes or anneals in different chemical systems over a wide range of conditions within the Earth's crust. Depending on the thermochemical factors pressure, temperature and chemical composition, impurities of trace metals and defect protons form different impurity-specific OH-defects that can qualitatively and quantitatively be analyzed by Fourier transform infrared (FTIR) spectroscopy. In general, proton incorporation follows the charge balance equation $[H^+]=[B^{3+}]+[Al^{3+}]-[Li^+]-[K^+]-[P^{5+}]$ (Bambauer 1961; Kats 1962; Müller and Koch-Müller 2009; Baron et al. 2015). The role of Li in this equation is more complicated, because it can be on either side of the equation and act both as an OH-defect forming species (such as LiOH) and an OH-defect reducing species that charge balances Al^{3+} (Frigo et al. 2016). Four major defect-types have been described that can be distinguished by their absorption frequency in the IR range: protons that are charge-balanced by Al^{3+} are responsible for an absorption triplet at 3310, 3378 and 3440 cm^{-1} wavenumbers (Kats 1962; Bambauer 1963), protons charge balanced by B^{3+} are responsible for an absorption band at 3595 cm^{-1} (Miyoshi et al. 2005; Müller and Koch-Müller 2009; Baron et al. 2015), and Li^+ is responsible for an absorption band at 3470-3480 cm^{-1} (Bambauer 1963; Aines and Rossman 1984). Another absorption band has been observed at 3585 cm^{-1} (Chakraborty and Lehmann 1976; Paterson 1986; Rovetta 1989). It occurs independent of metal impurities and is strongly dependent on water pressure (Stalder and Konzett 2012), and therefore most probably represents a silicon vacancy charged balanced by protons, i.e., hydrogarnet substitution ($Si^{4+}=4H^+$).

The OH-defects mentioned above have all been observed in natural samples, but averaged over the whole Earth's crust, the Al-specific OH-defect is by far most abundant, followed by the Li- and B-related defects (Stalder and Neuser 2013; Stalder 2014). The abundance of the hydrogarnet defect is present in small quantities in some quartz grains, but insignificant on a global scale.

Integral absorptions in the infrared range can be used to calculate absolute defect water concentrations using the calibrations of Aines et al. (1984), Libowitzky and Rossman (1997) or Thomas et al. (2009) that all result in very similar values for natural samples. A significant problem for the quantification of OH-defects are fluid micro-inclusions of molecular water which overlap the absorption bands caused by OH-defects and often are the most abundant hydrous species (Bambauer 1961; Müller and Koch-Müller 2009). Their abundances can be extremely variable within one single grain and their presence or absence usually is not an important characteristic of the formation conditions of an individual quartz grain. Polarized spectroscopic measurements for two vibrational directions on oriented grains are able to distinguish the anisotropic OH-defect signal from the isotropic water signal of the fluid inclusions, thus enabling the elimination of the fluid absorption signal. This procedure is possible, since the dipoles of nearly all OH-defects in quartz are aligned $||n_o$ enabling the distillation of the proper OH-defect signal by subtracting two polarised measurements (Stalder and Konzett 2012; Stalder and Neuser 2013; Baron et al. 2015).

In this study, systematic variations in the OH-defect speciation and content in granites and siliciclastic sediments (non-lithified such as recent river sediment and beach sand) and sedimentary rocks (lithified and metamorphosed such as quartzites) are statistically evaluated and their dependence on igneous, metamorphic and sedimentary processes are discussed. For the evaluation of metamorphic processes, thermal treatment at moderate pressures was performed.

Samples

Samples were chosen based on lithology, geological history and regional relation to each other (Table 1, Fig. 1 and 2). In this context, the granites from Sweden can be regarded as the main source of glacial deposits (Houmark-Nielsen and Kjær 2003) that today represent the siliciclastic material at the Baltic Sea coast (e.g., samples from Darß, Northern Germany). Similarly, granites from the Black

Forest are in the catchment area of the river Rhine (Fig. 2) and are important source rocks for the siliciclastic components of the sand fraction. Beside regional relations and their application to provenance analyses, this work is focused on the influence of thermal history. In this context, quartzites from two localities with different metamorphic conditions were studied, and, finally, the young (unmetamorphosed) granites from the Black Forest are compared to the Proterozoic granites of Sweden that suffered a long-lasting very low-grade to low-grade overprint.

Granites

Quartz single grains from 55 different granitic hand specimens and 4 light mineral separates from Sweden were derived from the rock sample collection of the Swedish Museum of Natural History in order to obtain a representative overview over a large part of the Proterozoic of the Fennoscandian shield (Fig. 1). Granites sampled from northern Sweden, and those in the vicinity of Stockholm, have Svecofennian ages (1.76-1.96 Ga), and the majority of these have been subjected to regional metamorphism. On the contrary, granites further south in the counties of Dalarna, Värmland (Filipstad granite) and Småland, represent the TIB suite of rocks (Transscandinavian Igneous Belt), which formed mainly around 1.8 Ga ago and are essentially undeformed. Two of the southernmost sample areas – the Vånga granite (Geisler and Schleicher 2000) and the Götemar granite (Söderlund et al. 2008) – have younger intrusion ages of 1.45 Ga and were not heated above 350°C after 1.4 Ga (Drake et al. 2009). Other samples from outside the Svecofennides include the 0.92 Ga old Bohus granite (Eliasson and Schöberg 1989), which formed during the Sveconorwegian (Grenvillean) thermotectonic event and is essentially undeformed, and the ca. 1.6 Ga old Uddevalla granite (Welin et al. 1982), which was metamorphosed during this event. Most of the prepared quartz grains from the Swedish granites showed undulose extinction under crossed nicols. Prominent exceptions (see Table 1) are samples from Dala granite (65108, 65109), Götemar granite (74026, 74027) and some samples from Vånga (72186-72190). Apart from the Vånga intrusion, two other large intrusions from Northern Sweden (~1.80 Ga Adak and ~1.85-1.89 Ga Jörn) were sampled at 10 different localities in order to investigate the homogeneity across these intrusions. The Jörn intrusion is a major batholith that comprises four different intrusive suites (GI – the oldest, to GIV, Wilson et al. 1987).

In addition to the Proterozoic granites from Sweden, 10 samples from the Seebach granite from the northern Black Forest (Fig. 2) were investigated. The Seebach granite is a Variscan S-type two-mica granite that was emplaced around 319 Ma ago (Hess et al. 2000) and was locally affected by syn-intrusive ductile extension (Grimmer et al. 2017). No post-intrusive deformation or thermometamorphic event is documented (Kalt et al. 2000).

Quartzites

The two quartzites analyzed are different with respect to age, geographical origin and metamorphic degree. The quartzite from the Hohe Tauern was derived from the Eclogite zone of the Tauern Window, Eastern Alps, Austria (sample A in Hoschek 2013). Initially deposited in the Mesozoic, the sediment was metamorphosed during Alpine plate collision and suffered peak metamorphic conditions of 600°C and 2 GPa (Hoschek 2013).

Two specimens of quartzite were sampled at the Vredefort dome, South Africa (Table 1). Both originate from an approximately 2.8 Ga old siliciclasic sequence from the Witwatersrand-Supergroup. Their post-shock (2.02 Ga) metamorphic conditions are estimated at ≤ 400°C (Gibson et al. 1997, Gibson 2002). As they were derived from the same metamorphic zone and did not show obvious differences in the OH-defect distribution from grain to grain, they were treated as one sample for better statistics.

Siliciclastic sediments

Sedimentary quartz samples were collected from the Rhine River close to the station of Rhöndorf, Germany, and the Baltic Sea beach close to the lighthouse Darßer Ort, Germany. The river sand from Rhöndorf consists of about 95% quartz (including the quartz from lithic fragments) and minor amounts of magnetite, diopside and glass. More than 90% of the material was in the grain size fraction of 125-500 µm, 8% were between 500 and 1000µm. The Rhine River is an example for a young large-scale drainage system (Fig.2). Sedimentary provenance studies show changing source contributions for Rhine sediments from Pliocene to Pleistocene, with a large fraction of Variscan and older rocks

indicated by zircon U-Pb ages (Krippner and Bahlburg 2013, Tatzel et al. 2017) and an Alpine contribution indicated by zircon (U-Th)/He and zircon fission track ages (Tatzel et al. 2017).

The sand sample from Darß is a very quartz-rich, well-sorted dune sand with >90% of grains in the 250-500 µm fraction. Siliciclastic material from the southern margin of the Baltic Sea consists of eroded material from Scandinavia, transported to its current location during the Pleistocene by the northern European inland ice sheet and released meltwater.

Experimental and analytical methods

Sample preparation

In natural quartz, the most abundant OH usually is hosted in melt, fluid (Bambauer 1961, Aines et al. 1984) and mineral (Stalder and Neuser 2013) inclusions. These inclusions are heterogeneously distributed, and isotropical or randomly oriented. Their contribution to the IR absorption spectra can be eliminated by subtracting two polarised measurements on oriented crystal sections with the E vector aligned in different crystallographic vibration directions (Stalder and Konzett 2012). OH-dipoles of hydrous defects are aligned perpendicular to the crystallographic c-axis and thus will not be biased by this procedure. Sections parallel to the c-axis were either prepared manually in a thermoplastic resin by the method described in Stalder and Neuser (2013), or measured on grain mounts or thick sections. Quartz crystals from granites were aligned and prepared manually from crushed and sieved hand specimens. After preparation, crystal sections were between 70 and 500µm thick (average 185 µm). The thickness was determined using a mechanical micrometer with a precision of ± 2 µm. Manual alignment was also performed for the 500-1000 µm fraction of the sand from Rhöndorf/Rhine. The 250-500 µm sand fraction from Rhöndorf/Rhine as well as the dune sand from Darß were prepared as grain mounts, and the quartzites were prepared as thick sections with a thickness of 110-120 µm. Optical orientation was checked by polarising microscopy using orthoscopic (birefringence $\Delta = 0.009$) and conoscopic illumination (flash figure).

IR spectroscopy

IR spectra were recorded at room temperature in transmission mode using a Bruker Vertex 70 FTIR spectrometer, coupled to a Hyperion 3000 microscope equipped with a liquid nitrogen-cooled MCT-detector, a globar light source, a KBr beamsplitter and a wire-grid IR-polariser and two polarisers for visible light. Measurements were performed with a spectral resolution of 2 cm^{-1} between 550 and 7500 cm^{-1}. Two measurements were performed on each grain with the vibrational electric E vector parallel to n_o, and parallel to n_e on exactly the same spot by turning the polarizer by 90 degree. After data acquisition spectral information was used to (1) omit minerals other than quartz, (2) check for the appropriate orientation, (3) eliminate the IR-signal for fluid, melt or mica inclusions by subtracting the spectra (n_o-n_e), and (4) check and – if appropriate – correct the thickness of the sample at the measured spot. Step (1) was rarely necessary, since minerals other than quartz usually were recognized prior to the IR measurement based on their optical properties. Step (3) is based on the fact that fluid and melt inclusions are isotropic and have the same absorption in both optical directions, while the OH-defects are nearly perfectly aligned parallel to n_o. In step (4) lattice overtones of all manually prepared crystals were used as a reference, because of their precisely determined orientation and thickness of each individual grain. After background correction, where each spectrum was vertically shifted to zero in the 2500-5000 cm^{-1} wavenumber range, the linear absorbance of the absorption band with the maximum at 1793 cm^{-1} (henceforth referred to as I_{1793}) measured parallel to the n_o vibration direction (occurring in all sections of quartz) correlates linearly with thickness up to 300 µm (Fig. 3). I_{1793} measured on grain mounts and thick sections were checked and corrected for a few grains, where a heterogeneous thickness was revealed. The numbers of successfully measured grains are given in Table 1. After subtracting a linear background between 3250 and 3600 cm^{-1}, OH absorption bands were used to quantify OH-defect concentrations using calibration of Libowitzky and Rossman (1997), where the linear absorbance measured at each wavenumber was multiplied with its wavelength-specific extinction coefficient and summed up over the OH absorption range. The total concentration was calculated from the absorption contributions 2(o-e), representing the two corrected contributions from the directions orthogonal to the c-axis, and taking into account that the third absorption component – the one parallel to n_e – was zero (Stalder and Neuser 2013). As molecular water from fluid inclusions, molecular water from and OH from melt inclusions, and the OH-signal from the

194 (mostly) randomly oriented mineral inclusions were eliminated in step (3), only OH vibrations from
195 point-defects were further considered. As OH point-defects in nominally anhydrous minerals are
196 commonly considered as "water" as the neutral chemical component, OH-defect contents are
197 expressed as wt ppm water (H_2O) equivalent.
198 The precision of the determined value for the OH content is estimated to ±10% if the main
199 error sources (background correction ±5%, thickness measurement ±2%, and other sources as
200 deviations from perfect orientation) are considered. Independent of the statistical error, the systematic
201 error based on the accuracy of the extinction coefficient is estimated to ±15-20% (Libowtzky and
202 Rossman 1997, Thomas et al. 2009).
203
204 **Thermal treatment in cold seal pressure vessels (CSPV)**
205 In order to monitor the evolution of hydrous defects in quartz during thermal treatment within the
206 Earth's crust, CSPV experiments between 1 and 3 kbar and 650-750°C with different fluid
207 compositions were performed (Table 2). Fragments of a crushed natural hydrothermal crystal
208 (unknown locality) were welded into Au-capsules with outer and inner diameters of 5.0 and 4.6 mm,
209 respectively. One set of experiments was nominally dry and contained additional powdered mica and
210 was performed close to the reaction curve Muscovite + quartz = K-feldspar + sillimanite + water. A
211 second set of experiments was performed with additional fine-grained quartz and calcite to produce a
212 CO_2-rich fluid. The reaction to wollastonite + quartz was checked by weighing, piercing and
213 reweighing the capsule after each run. In one run (QzWo02), 2µl water was added to the experimental
214 charge with a microsyringe, otherwise the starting material was kept dry and no water was added. Au-
215 capsules were sealed using a Lampert PUK U3 welding device (equipped with tungsten electrode,
216 flushed with argon gas). Pressure treatment was performed in Rene 41 steel cold seal pressure vessels
217 using water as pressure medium. Temperature was measured by Ni-CrNi thermocouples, pressures
218 were measured with a Heise gauge and kept constant within 0.1 kbar during the whole run duration. In
219 order to further confirm the wollastonite-reaction, some charges were investigated under the SEM with
220 an acceleration voltage of 15 kV using a JEOL JSM-6010LV instrument (Fig. 4).
221

Results

IR-spectra from granitic quartz grains from the Black Forest (Fig. 5a) exhibit Al- and Li-specific OH-defects at 3378 and 3480 cm^{-1}, respectively; one grain also shows a significant absorption band at 3595 cm^{-1}, indicative for B-related OH-defects. With respect to the Al/Li-specific bands, subtle but significant variations from one grain to another are observed, and the total absorbance is variable within a factor of two. A systematic link between the observed changes in spectral characteristics and the position within the outcrop could not be established. In contrast to samples from the Black Forest, Li- and B-related OH-defects do not contribute significantly to the total absorption in granitic quartz grains from Sweden (Fig. 5b). Apart from two localities (Vånga and Götemar) the mean OH absorption band at 3378 cm^{-1} is small, too.

Average IR-spectra from quartz grains from the quartzites from Vredefort and Hohe Tauern (Fig. 6) are in most respects similar to the granitic quartz grains from the Swedish granite samples. The OH absorption bands are small, with the largest OH band appearing at 3378 cm^{-1}. For comparison, the evolution of IR-spectra during thermal treatment in the CSPV at metamorphic conditions is also shown in Fig. 6. Compared to the natural untreated quartz, annealing always led to a decrease of the 3480 cm^{-1} absorption band compared to the 3378 cm^{-1} absorption band, resulting in IR-spectra dominated by Al-specific OH bands (in agreement with Kronenberg et al. 1986).

IR-spectra from sedimentary quartz grains show a large variability both in terms of absorbance and spectral shape. Quartz grains from the sediment from Rhöndorf/Rhine exhibit Al-, Li-, and B-related OH-defects in a broad range of band ratios (Fig. 7a), and average spectra exhibit rather high absorbances and significant Li- and B-related bands. In contrast, the average grain of the beach sediment from Darß is rather poor in OH-defects (Fig. 7b), even though individual grains show very strong OH absorption bands and significant contributions of Li- or B-related OH bands.

Total OH-defect concentrations are displayed as histograms in Fig. 8. Most of the granites from Sweden have quartz with low OH-defect concentrations (equivalent to < 5 wt ppm H_2O). Most grains

are in the class 2-3 wt ppm water, and it is unclear, whether there is a unimodal or bimodal distribution within this low-water class. However, if individual concentrations of all samples are considered, there seems to be a minimum around 2 wt ppm and maxima close to 1 and 3 wt ppm (Fig. 8a). Another minor mode – representing the granites from Götemar and Vånga – occurs around 15 wt ppm water as OH-defects. Here again, it is unclear whether the minimum at 10 wt ppm is real or whether this gap would be closed if more samples were analyzed. The quartzites from the Hohe Tauern and Vredefort have similar average defect water concentrations, but exhibit enormous differences in the defect distribution from grain to grain (Fig. 8b,c). Whilst the distribution for the sample from the Hohe Tauern is in accord with a Gaussian function (with an error of 25%), the sample from Vredefort shows a very uneven distribution that cannot be explained by statistical error. The two grain size fractions from the Rhine River sediment (Fig. 8d,e) both show polymodal distribution with maxima around 20 and 40 wt ppm, whilst the beach sediment from Darß (Fig. 8f) exhibits only one mode at very low defect water concentrations with significant contributions from high to very high values (up to 114 wt ppm, Table 1 and Fig. 7b).

Discussion

In order to interpret the data in a broad geological context, we have to consider several different processes that may have generated (and later influenced) the defect chemistry. The final sample's spectral characteristics may be the result of a long complex geological history comprising igneous, metamorphic and sedimentary processes. The following aspects will be evaluated here: 1) defect incorporation under igneous conditions during progressive crystallization and differentiation, 2) thermal annealing and diffusion processes during metamorphic overprint, 3) influence of OH-defects on mechanical properties and their consequences for transport and weathering.

A promising starting point to study the different processes separately is therefore the investigation of young igneous samples. In contrast, old igneous rocks may have suffered thermal or deformational overprinting, which may add further complexities. Similarly, hydrous defects in metamorphic rocks may reflect an intermediate state somewhere between the original protolith and the fully annealed sample.

Sediments and sedimentary rocks are still more complex as they represent a mixture of different sources that may contain grains from igneous, metamorphic (and remobilized sedimentary) quartz and can only be evaluated if igneous and metamorphic defects are defined.

Variations within igneous and hydrothermal systems

If in thermodynamic equilibrium, OH incorporation depends on thermochemical parameters such as pressure, temperature and chemistry of the system (Stalder and Konzett 2012; Baron et al. 2015; Frigo et al. 2016). Therefore, variation in the OH-defects chemistry in quartz grains within one igneous body reflect changes in the melt composition during progressive crystallization and/or partitioning behavior of impurities between quartz and melt. Experimental studies have shown that B- and Li-specific OH-defects in quartz reflect variable melt compositions until saturation of an accessory phase such as tourmaline or spodumene is reached (Baron et al. 2015, Frigo et al. 2016). The respective absorption bands, e.g., expressed as $(I_{3480}+I_{3595})/I_{3378}$, thus should define arrays that are typical for the prevailing crystallization conditions. Quartz crystals from the Black Forest granites define a rough trend (Fig. 9) that is similar – though shifted to lower water contents – to the experimentally produced trend in a spodumene-bearing granite at 10 kbar (Frigo et al. 2016). Within the trend of these quartz crystals from the Black Forest granite, the majority of the crystals plot on the water-rich and Al-rich ($(I_{3480}+I_{3595})/I_{3378}=0.5$) margin of the cluster. According to the experimental results of Frigo et al. (2016), the opposite margin of the cluster ($c_{H2O}<20$ wt ppm, $(I_{3480}+I_{3595})/I_{3378}=0.8$) may be interpreted as igneous pulses or crystallization stages closer to the saturation in a Li- and B-bearing accessory phase.

Variations in the OH-defect chemistry may also occur on the microscale (Bambauer 1961; Müller et al. 2003, 2009), as illustrated here by the hydrothermal quartz fragments used for the CSPV runs (see methods section) that range from 0-25 wt ppm water. They define their own variation array in Fig. 9, revealing drastic changes of the hydrothermal fluid composition during progressive crystallization.

The OH-defect content in the Proterozoic granitic bodies from Sweden is generally very low. Moderate OH-defect contents (between 10 and 20 ppm) were observed in the Dala granite, the Götemar granite and the Vånga granite. The latter two differ from most other granites in Scandinavia,

306 representing a significantly younger igneous event. Their age ranges around 1.45 Ga (Geisler and
307 Schleicher 2000; Söderlund et al. 2008) coincident with the last metamorphic event of the
308 Transscandinavian igneous belt (TIB) to which they belong. However, a later metamorphic event
309 occurred during the Sveconorwegian event centered in the west of TIB (Geisler and Schleicher 2000).
310 Interestingly, the most western sample from Vånga showed the lowest defect water content (Table 1),
311 illustrating the effect of water loss during the thermal event. Preferential defect-water loss at the rim of
312 igneous bodies is also observed in the Adak and Jörn granite. In case of Adak granite, the NW-SE
313 profile along an outlet tunnel for a hydro-electric power plant shows significant higher defect water
314 contents in quartz towards the center of the igneous body (Fig. 10) and low defect water contents
315 towards the (western) rim. The pattern observed in the Jörn pluton is much more complex. There is a
316 tendency that higher water contents are found in the center (Fig. 11), but is has to be taken into
317 account that Jörn consists of different igneous pulses (GI-GIV). GI has generally very low hydrous
318 defect contents, whereas the later pulses GII and GIII have generally more variable OH contents. GI
319 may have lost hydrous defects during the later GII-GIV events, which in turn allowed the defects to be
320 retained at the center of the igneous complex.
321
322 **Hydrous defects during metamorphism**
323 Based on the present data set, it cannot be determined unequivocally whether hydrous defects are
324 destroyed by deformation or by chemical diffusion during heating. The qualitative correlation between
325 undulose extinction and hydrous defect content suggests that quartz grains that suffered post-
326 crystallization deformation (and metamorphism) lost defect water.
327 The systematic zonation of the hydrous defects content in the igneous bodies mentioned in the
328 previous section, in particular their low water content towards the rim of the body, does not reflect
329 original igneous water content. Quantitative data concerning grain boundary diffusion of water in
330 granites are not available in the literature, but we can assume that they are orders of magnitude faster
331 than hydrogen diffusion in quartz (e.g., Kats 1962; Kronenberg and Kirby 1987), and a large igneous
332 body could partly preserve its defect water in the center, but could be partially dehydrated at the rim
333 within several Ma at low grade metamorphic conditions. Based on thermochemical considerations, this

334 value is not expected to decrease to zero, given that nominally water-bearing phases (mica and fluid
335 and melt inclusions) are present.
336
337 The different defect distribution in the quartzites studied here may be interpreted in terms of their
338 metamorphic history. Variations in hydrous defect contents are preserved in the low-grade quartzites
339 from Vredefort (Fig. 8c) while hydrous defect concentrations within the high-grade quartzite from the
340 Hohe Tauern are uniform within statistical error (Fig. 8b), and may be explained by high-temperature
341 diffusional annealing of the hydrous point defects. It is unlikely that hydrous defects, as observed in
342 the Hohe Tauern quartzite, represent the distribution in the precursor sandstone, since so far no
343 sediments with such a well-equilibrated grain-to-grain distribution have been described (Stalder and
344 Neuser 2013; Stalder 2014). In contrast, the grain-to-grain variations of hydrous defects in the quartz
345 crystals from Vredefort may represent the precursor sandstone whose grains were derived from
346 sources consisting of a large fraction of metamorphosed terranes. Alternatively, the low average
347 content in hydrous defects may be connected to the shock-metamorphism, where all grains lost some
348 water. Though, neither the shock-metamorphism nor the subsequent long-term low-grade regional
349 metamorphism was able to equilibrate the OH content between the quartz grains.
350 If the accumulated number of grains is plotted against the defect water content in a double logarithmic
351 diagram, both quartzite samples define trends with different slopes (Fig. 12). A steeper slope indicates
352 a smaller variability in hydrous defects from one grain to another and, in the case of low defect
353 contents of the quartzite, can be interpreted as equilibrium values at higher metamorphic conditions. In
354 general, Al-specific OH-defects seem to be more stable than B- and Li-related, which is documented
355 by the dominance of Al-related OH-defects in quartzites, meta-granites and the run products from the
356 CSPV experiments (Fig. 5b and 6). It can also be concluded that at 350-400°C, Al-related OH point-
357 defects are destroyed very slowly and are probably stable over geological timescales below 300°C.
358 According to the observations on metamorphic rocks and as suggested from sandstones that suffered
359 diagenetic temperatures of 150-200°C (Aldahan 1985), low temperature processes such as
360 sedimentation and diagenesis are not expected to change the nature of the incorporated OH-defects in
361 quartz (Stalder 2014).

Application as tool for provenance analysis

Quartz grains from the beach sand from Darß/Germany (with an average of 4 wt ppm) are amongst the most water-poor samples in sedimentary material. In contrast, the river sand from Rhöndorf/Rhine belongs (with an average of >20 wt ppm) to the most water-rich sedimentary sample (compared with samples of Stalder 2014). Interestingly, these values correlate well with the analyzed granites from their source area (Fig. 2), namely an average of 4 wt ppm water for the Swedish granites and 24 wt ppm water for the granites from the Black Forest (Table 1). Summarizing, it appears that sedimentary quartz grains in Middle Europe (Fig. 2) have dry source rocks to the North and wet source rocks to the South with significant hydrous defect concentrations. This interpretation holds for older sedimentary material: Triassic sandstones in Germany have average hydrous defect contents of 18 wt ppm (Stalder 2014) and – similar to the Rhine River today – received substantial amounts of siliciclastic material from Variscan and some older sources (Paul et al. 2008). We are aware that the data set is not complete yet, and that the sources of these sediments do not consist exclusively of the granites analysed here (and not exclusively of granites at all). Therefore histograms for Darß and Swedish granites are not identical (Fig. 8a,f).

Based on their spectral characteristics, quartz grains from individual sources define spectral clusters (Fig. 9) that may be related to grain clusters observed in a siliciclastic sediment, and thus may help to identify distinct sources. Furthermore, hydrous defects in quartz can serve to constrain provenance of quartz grains with respect to the prevailing rock types in the source region (e.g., old metamorphosed granite such as in Scandinavia or relatively young granites in the case of Black Forest). It further may be of interest that Proterozoic rocks from Scandinavia represent a considerably deeper crustal section than the young rocks from the Variscan orogeny. This fits in our interpretation, too, because experimental results suggest that the quantity of hydrous defects decreases with pressure (Stalder and Konzett 2012; Baron et al. 2015), and quartz in lower crustal sections thus should generally exhibit lower hydrous defect contents.

Using hydrogen defect concentrations to identify sources of sediments may suffer from the same problems as other provenance indicators, for example, the source rocks may have been eroded. Old

sandstones such as the 1.4 Ga old Dala sandstone from Sweden (Aldahan 1985; Pulvertaft 1985) fed from the Proterozoic Fennoscandian Shield when it still was young, are therefore important archives. Quartz grains from the Dala sandstone exhibit much higher hydrous defect contents than observed in rocks from the present surface (Stalder 2014), indicating that the upper part of the Svecofennides was much more hydrous when the material of the Dala sandstone was deposited.

Implications

At high-temperatures (igneous conditions), incorporation of OH-defects in quartz is primarily controlled by thermodynamic parameters and reflects the conditions of the environment where the respective quartz crystals were formed. In contrast, at low temperatures, rates of diffusion are generally too slow for hydrous defects to attain the new equilibrium. Thus, a quartz crystal with a complex geological history may exhibit defect chemistry that reflects different conditions of its geological history and analysis of a single grain (on a single spot) is not meaningful. In contrast, a statistical treatment of a large number of grains may define distribution curves and spectral trends that provide information on several sedimentary, metamorphic and/or igneous events. Future studies may focus on (1) more detailed experimental studies to link hydrous defects in quartz to quantitative petrological formation conditions, (2) apply the experimental findings to document changes in crystallization conditions in large igneous bodies and (3) link quartz grains from sediments to their source rocks.

Acknowledgements

This study was supported by the Austrian Science Fund (FWF): P29145-N34 and the SYNTHESYS program (project SE-TAF-5762). We further would like to acknowledge the donation of the samples from the Black Forest from VSG Schwarzwald-Granit-Werke GmbH (D-76596 Forbach-Raumünzach), and some of the Swedish samples were initially sampled by the Geological Survey of Sweden. Franz Gartner is thanked for the preparation of the grain mounts and Martina Tribus for help with the SEM. Per-Olof Persson is thanked for providing light mineral separates. Andreas Kronenberg and an anonymous reviewer are thanked for thorough and constructive comments.

418

419 References

420 Aldahan, A.A. (1985) Mineral diagenesis and petrology of the Dala sandstone. Bulletin of the
421 Geological Institute Uppsala University, 12, 1–48.

422 Aines, R.D., and Rossman, G.R. (1984). Water in minerals? A peak in the infrared. Journal of
423 Geophysical Research, 89, 4059–4071.

424 Aines, R.D., Kirby, S.H., and Rossman, G.R. (1984) Hydrogen speciation in synthetic quartz.
425 Physics and Chemistry of Minerals, 11, 204–212.

426 Bambauer, H.U. (1961) Spurenelementgehalte und γ-Farbzentren in Quarzen aus Zerrklüften der
427 Schweizer Alpen. Schweizerische Mineralogisch Petrographische Mitteilungen, 41, 335–369.

428 Bambauer, H.U. (1963) Merkmale des OH-Spektrums alpiner Quarze (3μ-Gebiet). Schweizerische
429 Mineralogisch Petrographische Mitteilungen, 43, 259–268.

430 Baron, M.A., Stalder, R., Konzett, J., and Hauzenberger, C.A. (2015) OH-point defects in quartz in B-
431 and Li-bearing systems and their application to pegmatites. Physics and Chemistry of
432 Minerals, 42, 53–62.

433 Biró, T., Kovács, I.J., Király, E., Falus, G., Karátson, G., Bendö, Z., Francsik, T., and Sándorné, K.
434 (2016): Concentration of hydroxyl defects in quartz from various rhyolitic ignimbrite
435 horizons: results from unpolarized micro-FTIR analyses on unoriented phenocryst fragments.
436 European Journal of Mineralogy, 28, 313–327.

437 Chakraborty, D., and Lehmann, G. (1976) Distribution of OH in synthetic and natural quartz crystals.
438 Journal of Solid State Chemistry, 17, 305–311.

439 Drake, H., Tullborg, E.L., and Page, L. (2009) Distinguished multiple events of fracture mineralization
440 related to far-field orogenic effects in Paleoproterozoic crystalline rocks, Simpevarp area, SE
441 Sweden. Lithos, 110, 37–49.

442 Ehlers, J., Meyer, K.D., and Stephan, H.J. (1984) The pre-Weichselian glaciations of North-West
443 Europe. Quaternary Science Reviews, 3, 1–40.

444 Eissmann, L. (1986): Quartärgeologie und Geschiebeforschung im Leipziger Land mit einigen

Schlußfolgerungen zu Stratigraphie und Vereisungsablauf im Norddeutschen Tiefland, p. 105-133. In: Richter, E., Baudenbacher, R., Eissmann, L. (Eds.): Die Eiszeitgeschiebe in der Umgebung von Leipzig. Bestand, Herkunft, Nutzung und quartärgeologische Bedeutung, 3, p. 105–133. Altenburger Naturwissenschaftliche Forschung, Naturkundliches Museum Mauritianum, Altenburg (in German).

Eliasson, T., and Schöberg, H. (1989) U-Pb dating of the post-kinematic Sveconorwegian (Grenvillian) Bohus granite, SW Sweden – evidence of restitic zircons. Precambrian Research, 51, 337–350.

Frigo, C., Stalder, R., and Hauzenberger, C.A. (2016) OH-defects in quartz in granitic systems doped with spodumene, tourmaline and/or apatite: experimental investigations at 5-20 kbar. Physics and Chemistry of Minerals, 43, 717–729.

Geisler, T., and Schleicher, H. (2000) Composition and U-Th-total Pb model ages of polygenetic zircons from the Vånga granite, south Sweden: An electron microprobe study. Geologiska Föreningens i Stockholm Förhandlingar (GFF), 122, 227–235.

Gibson, R.L. (2002) Impact-induced melting of Archean granulites in the Vredefort Dome, South Africa. I: anatexis of metapelitic granulites. Journal of Metamorphic Geology, 20, 57–70.

Gibson, R.L., Reimold, W.U., and Wallmach, T. (1997) Origin of pseudotachylite in the lower Witwatersrand Supergroup, Vredefort Dome (South Africa): constraints from metamorphic studies. Tectonophysics, 283, 241–262.

Grimmer, J.C., Ritter, J., Eisbacher, G.H., and Fielitz, W. (2017) The late Variscan control on the location and assymmetry of the Upper Rhine Graben. International Journal of Earth Sciences, 106, 827–853.

Hess, J.C., Hanel, M., Arnold, M., Gaiser, A., Prowatke, S., Stadler, S., and Kober, B. (2000) Variscan magmatism at the Northern margin of the Moldanubian Vosges and Schwarzwald I. Ages of intrusion and cooling history. Beihefte zum European Journal of Mineralogy, 12, 79.

Hoschek, G. (2013) Garnet zonation in metapelitic schists from the Eclogite Zone, Tauern Window, Austria: comparison of observed and calculated profiles. European Journal of Mineralogy, 25, 615–629.

473 Houmark-Nielsen, M., and Kjær, K.H. (2003) Southwest Scandinavia, 40-15 kyr BP: palaeogeography
474 and environmental change. Journal of Quaternary Science, 18, 769–786.
475 Kalt, A., Altherr, R., and Hanel, M. (2000) The variscan basement of the Schwarzwald. Beiheft 2
476 European Journal of Mineralogy, 12, 1–43.
477 Kats, A. (1962) Hydrogen in alpha quartz. Philips Research Reports, 17, 133–279.
478 Korja, A., and Heikkinen, P. (2005) The accretionary Svecofennian orogeny – insight from the
479 BABEL profiles. Precambrian Research, 136, 241–268.
480 Krippner , A., and Bahlburg, H. (2013) Provenance of Pleistocene Rhine river middle terrace sands
481 between the Swiss-German border and Cologne based on U-Pb detrital zircon ages. I
482 nternational Journal of Earth Sciences, 102, 917–932.
483 Kronenberg, A.K., and Kirby, S.H. (1987) Ionic conductivity of quartz: DC time dependence and
484 transition in charge carriers. American Mineralogist, 72, 739–747.
485 Kronenberg, A.K., Kirby, S.H., Aines, R.D., and Rossman, G.R. (1986) Solubility and diffusional
486 uptake of hydrogen in quartz at high water pressures: implications for hydrolytic weakening.
487 Journal of Geophysical Research, 91B, 12723–12744.
488 Libowitzky, E., and Rossman, G.R. (1997) An IR calibration for water in minerals. American
489 Mineralogist, 82, 1111–1115.
490 Miyoshi, N., Yamaguci, Y., and Maino, K. (2005) Successive zoning of Al and H in hydrothermal
491 vein quartz. American Mineralogist, 90, 310–315.
492 Müller, A., and Koch-Müller, M. (2009) Hydrogen speciation and trace element contents of igneous,
493 hydrothermal and metamorphic quartz from Norway. Mineralogical Magazine, 73, 569–583.
494 Müller, A., Wiedenbeck, M., van den Kerkhof, A.M., Kronz, A., and Simon, K. (2003) Trace elements
495 in quartz – a combined electron microprobe, secondary ion mass speactrometry, laser ablation
496 ICP-MS, and cathodoluminescence study. European Journal of Mineralogy, 15, 747–763.
497 Müller, A., van den Kerkhof, A.M., Behr, H.-J., Kronz, A., and Koch-Müller, M. (2009) The evolution
498 of late-Hercynian granites and rhyolites documented by quartz – a review. Earth and
499 Environmental Science Transactions of the Royal Society of Edinburgh, 100, 185–204.
500 Paul, J., Wemmer, K., and Ahrendt, H. (2008) Provenance of siliciclastic sediments (Permian to

Jurassic) in the Central European Basin. Zeitschrift der Deutschen Gesellschaft für Geowissenschaften, 159, 641–650.

Paterson, M.S. (1986) The thermodynamics of water in quartz. Physics and Chemistry of Minerals, 13, 245–255.

Pulvertaft, T.C.R. (1985). Aeolian dune and wet interdune sedimentation in the Middle Proterozoic Dala sandstone, Sweden. Sedimentary Geology, 44, 93–111.

Rovetta, M.R., Holloway, J.R., and Blacic, J.D. (1986) Solubility of hydroxyl in natural quartz annealed in water at 900°C and 1.5 GPa. Geophysical Research Letters, 13, 145–148.

Söderlund, P., Page, L., and Söderlund, U. (2008) $^{40}Ar/^{39}Ar$ biotite and hornblende geochronology from the Oskarshamn area, SW Sweden: discerning multiple Proterozoic tectonothermal events. Geological Magazine, 145, 790–799.

Stalder, R. (2014) OH-defect content in detrital quartz grains as an archive for crystallization conditions. Sedimentary Geology, 307, 1–6.

Stalder, R., and Konzett, J. (2012) OH-defects in quartz in the system quartz – albite – water and granite – water between 5 and 25 kbar. Physics and Chemistry of Minerals 39, 817–827.

Stalder, R., and Neuser, R.D. (2013). OH-defects in detrital quartz grains: potential for application as tool for provenance analysis and overview over crustal average. Sedimentary Geology, 294, 118–126.

Stephan, H.J. (2001) The Young Baltic advance in the western Baltic depression. Geology Quarterly, 45, 359–363.

Tatzel, M., Dunkl, I., and von Eynatten, H. (2017) Provenance of Palaeo-Rhine sediments from zircon thermochronology, geochemistry, U/Pb dating and heavy mineral assemblages. Basin Research, 29, 396–417.

Thomas, S.M., Koch-Müller, M., Reichart, P., Rhede, D., Thomas, R., and Wirth, R. (2009) IR calibrations for water determination in olivine, r-GeO_2 and SiO_2 polymorphs. Physics and Chemistry of Minerals, 36, 489–509.

Welin, E., Einarsson, Ö., Gustafsson, B., Lindberg, R., Christiansson, K., Johansson, G., and Nilsson,

Ö. (1977). Radiometric ages of intrusive rocks in Northern Sweden II. Sveriges Geologiska Undersökning, Yearbook 71 (6), 1–21.

Welin, E., Gorbatchev, R., and Kähr, A.-M. (1982) Zircon dating of the polymetamorphic rocks in southwestern Sweden. Sveriges Geologiska Undersökning, C797, 38 p.

Wilson, M.R., Sehlstedt, S., Claesson, L.Å., Smellie, J.A.T., Aftalion, M., Hamilton, P.J., and Fallick, A.E. (1987) Jörn: an early Proterozoic intrusive complex in a volcanic-arc environment, North Sweden. Precambrian Research, 36, 201–225.

Ziegler, P.A., 1990. Geological Atlas of Western and Central Europe. Shell Internationale Petroleum Maatschappij B.V., The Hague, 239 p.

Figure Captions

Figure 1: Geographical overview over the investigated granites from Sweden. Squares indicate localities where samples were collected. The size of the symbol correlates to the number of specimens that were analyzed from the respective locality (see Table 1). Borders between geological units are simplified after Korja and Heikkinen (2005). The age indicated for *Sveconorwegian* refers to the orogenesis, but many rocks in the *Sveconorwegian province* are older (up to 1.6 Ga). TIB = Transscandinavian Igneous Belt.

Figure 2: Geographical overview over the samples from Germany (Table 1). D = Darß, R = Rhöndorf/Rhine, G = granite quarry (Black Forest), BF = Black Forest. Broken lines with arrows indicate transport directions during the last glacial period (after Ehlers et al. 1984, Stephan 2001) and dotted curves with arrows represent transport direction during previous Pleistocene glaciations (after Eissmann 1986). Short arrows indicate transport direction during the lower Triassic (after Ziegler 1990).

Figure 3: (a) IR spectra of lattice overtones from oriented quartz sections measured with E parallel to the vibrational direction n_o. The band at 1793 cm^{-1} is most promising to determine the thickness of the crystal section, because this band is not very sensitive to orientation and less absorbing than the other overtones. Spectra are slightly offset for graphical reasons. (b) Correlation of the linear absorbance at 1793 cm^{-1} and thickness. Below 300 µm thickness I_{1793} can be used to check the thickness and correct the mechanical measured value. For thicker samples, radiation is nearly totally absorbed, leading to a truncation of the absorption band. The limitation of the linear correlation to 300 µm is in good agreement with Biró et al. (2016) for unpolarized measurements on unoriented quartz crystals, although the polarized measurements presented here show a significantly higher R^2 (0.96 versus 0.86).

Figure 4: SEM image of the experimental charge QzWo04. The wollastonite needles (Wo) formed from the reaction of quartz and calcite, which produced a CO_2-rich fluid phase.

Figure 5: IR spectra (n_o-n_e) from quartz from the granites from (a) Black Forest and (b) Sweden. Spectra are normalized by thickness and vertically offset for graphical reasons.

Figure 6: IR spectra (n_o-n_e) from quartz from the CSPV runs compared to IR spectra from natural

quartzites (average over all measured spectra) from the Hohe Tauern, Austria and Vredefort, South Africa. Spectra are normalized by thickness and vertically offset for graphical reasons. "Qz natural" refers to the natural hydrothermal quartz used as starting material for the CSPV runs. Its OH-content was highly variable (see Figure 9), but all spectra were self-similar. The spectrum exhibited here is an average of 7 measured fragments.

Figure 7: IR spectra (n_o-n_e) from selected grains from siliciclastic sediments from (a) Rhöndorf/Rhine, Germany and (b) Darß, Germany. Average spectra are shown as thick lines. Spectra are normalized by thickness and vertically offset for graphical reasons.

Figure 8: Histograms showing the statistical distribution of defect water in quartz in (a) the granites from Sweden, (b) the quartzite from the Hohe Tauern, (c) the quartzite from Vredefort, (d, e) the 250-500 µm and 500-1000 µm fraction from the Rhine River sediment from Rhöndorf, (f) the 250-500 µm fraction from the beach sand from Darß. The solid curve in (a), (d), (e) and (f) represents the sum of all analyzed grains, where the water concentration of each individual grain is considered as a probability curve (Gaussian function). For the quartzite samples (b-c) the solid curve represent the average ± standard deviation over all grains.

Figure 9: Spectral characteristics plotted as $(I_{3595}+I_{3480})/I_{3378}$ against absolute OH-defect content. Grains with significant contributions of Li- and/or B-specific OH-defects plot at higher values for $(I_{3595}+I_{3480})/I_{3378}$. Quartz grains from the sediment from Rhöndorf/Rhine (cicles) are displayed as two groups representing grains with strong contributions of B-specific defects ($I_{3595}/I_{3480} > 0.7$, filled circles) and those with lower contributions of B-specific defects ($I_{3595}/I_{3480} < 0.7$, open circles). The broken ellipse labeled F16 shows the trend for experimentally grown quartz in a spodumene-bearing granite at 10 kbar (Frigo et al. 2016). Grains from the Black Forest granite (see also spectra in Fig. 5a) are encircled by the dotted line for better clarity.

Figure 10: Defect water contents along an outlet tunnel from the hydro-electric power plant from Adak (Northern Sweden, see Table 1). The dashed lines indicate the rim of the igneous body (Welin et al. 1977).

Figure 11: Geological sketch of the Jörn granite intrusion with defect water contents in quartz in wt

ppm water. Different colors indicate different intrusion phases (modified after Wilson et al. 1987).

Figure 12: Double-logarithmic plot of % grains against defect water content. Contents below 1 ppm are not plotted due to large uncertainty of these low values. Error bars given for the sediment samples from Rhöndorf/Rhine (250-500 µm and 500-1000 µm size fraction) represent 10% analytical error for single grain analysis. Both samples show small, but significant differences. The black line represents the global average estimated from Stalder (2014).

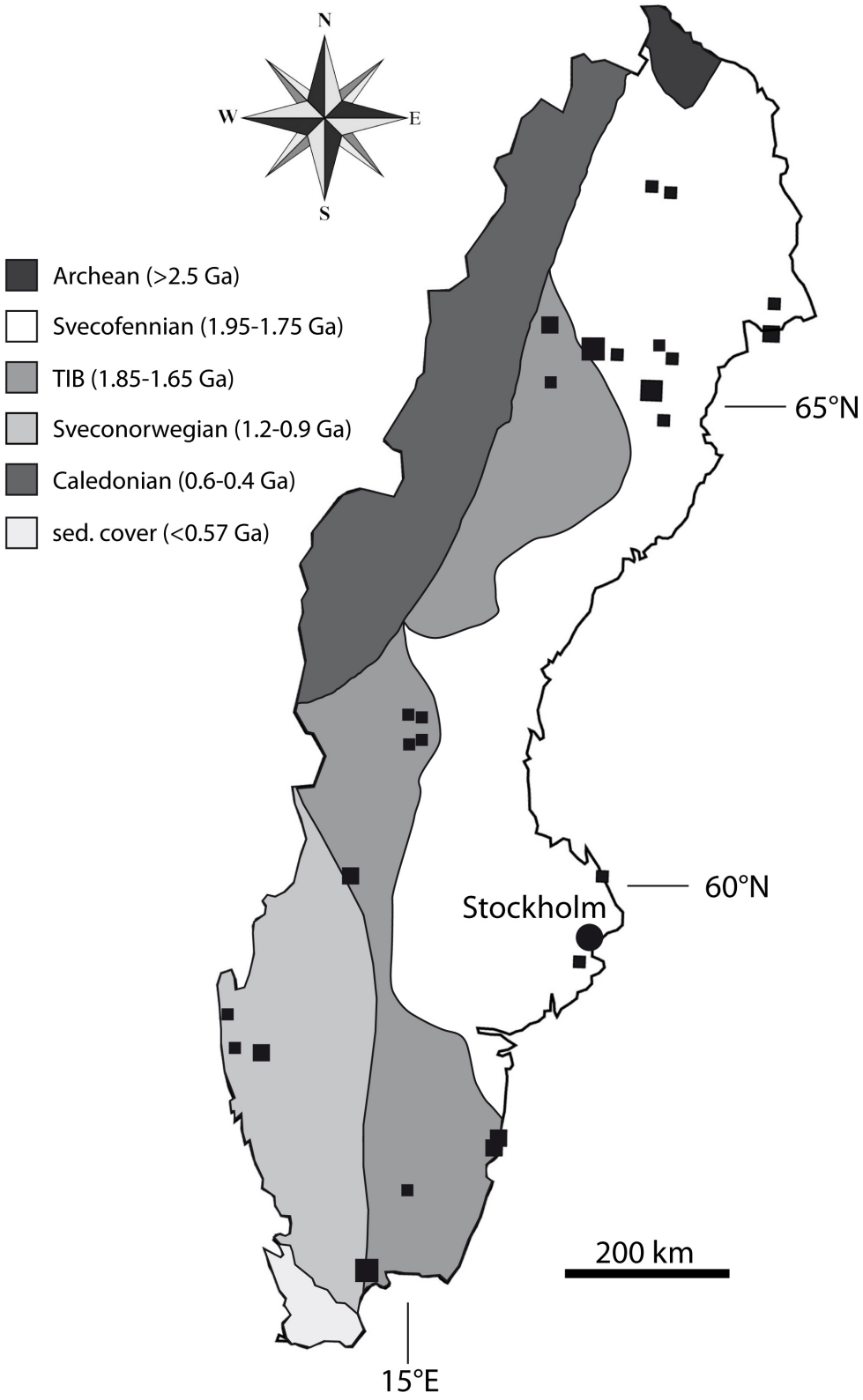
N
W
E
S
Archean (>2.5 Ga)
Svecofennian (1.95-1.75 Ga)
TIB (1.85-1.65 Ga)
Sveconorwegian (1.2-0.9 Ga)
Caledonian (0.6-0.4 Ga)
sed. cover (<0.57 Ga)
65°N
60°N
Stockholm
200 km
15°E

Figure 1

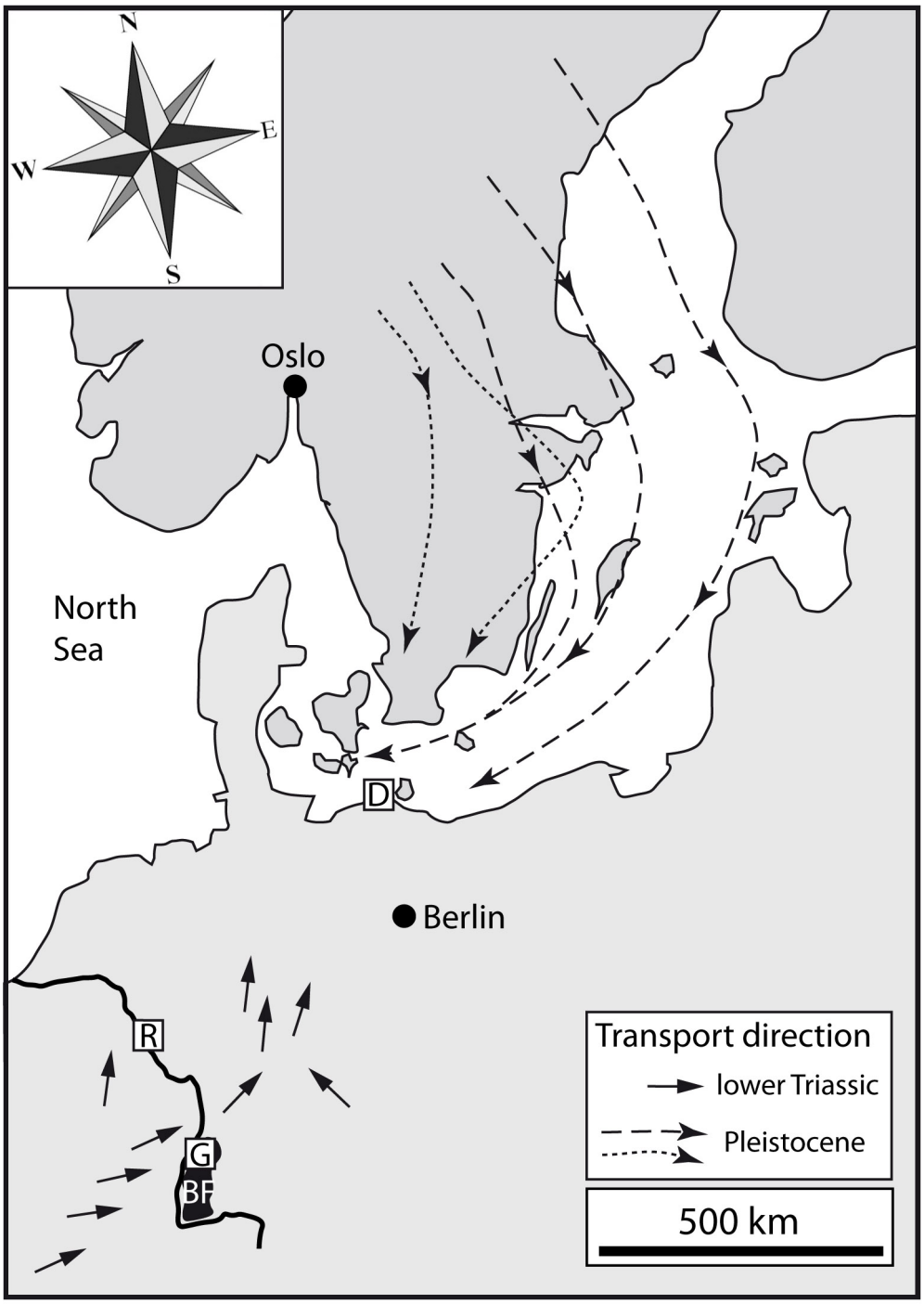
N
E
W
S
Oslo
North
Sea
D
Berlin
R
G
BF
Transport direction
lower Triassic
Pleistocene
500 km

Figure 2

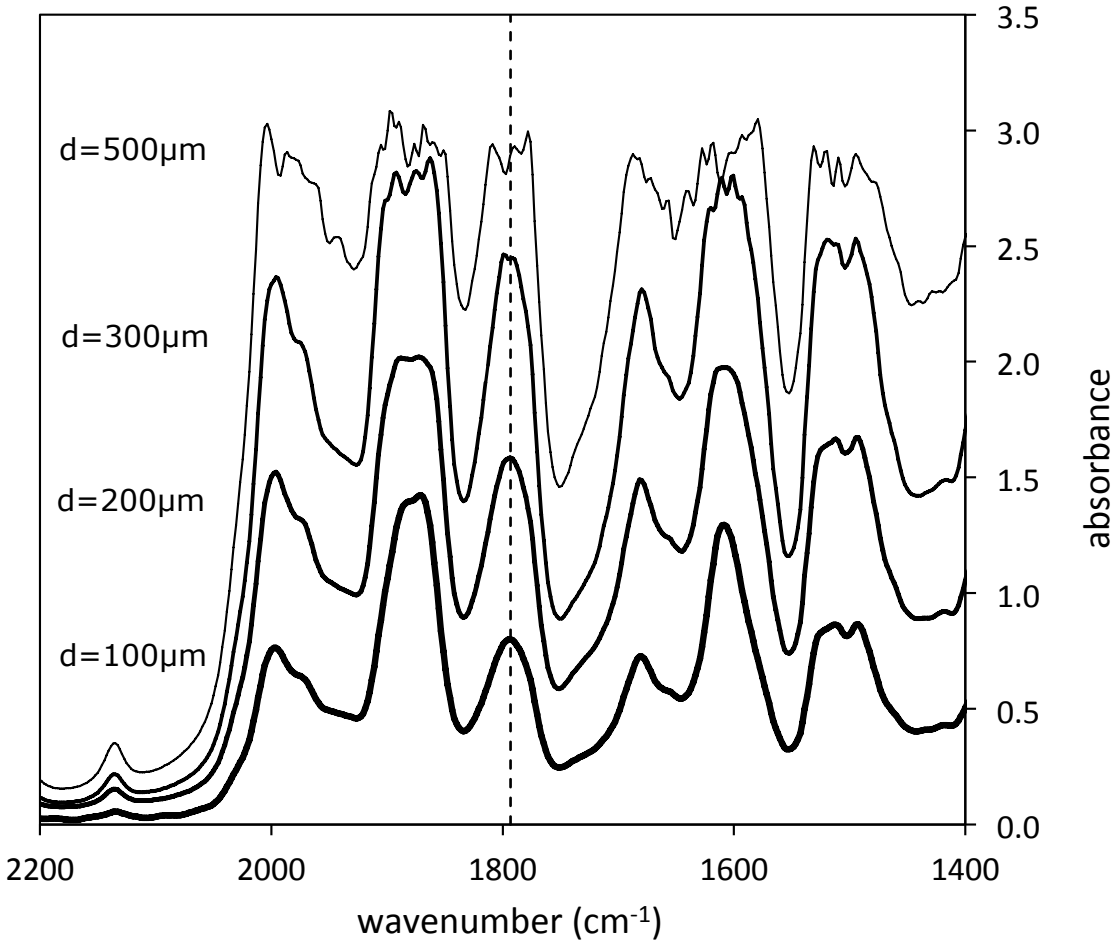
d=500µm
d=300µm
d=200µm
d=100µm
3.5
3.0
2.5
2.0
1.5
1.0
0.5
0.0
absorbance
2200
2000
1800
1600
1400
wavenumber (cm-1)

Figure 3a

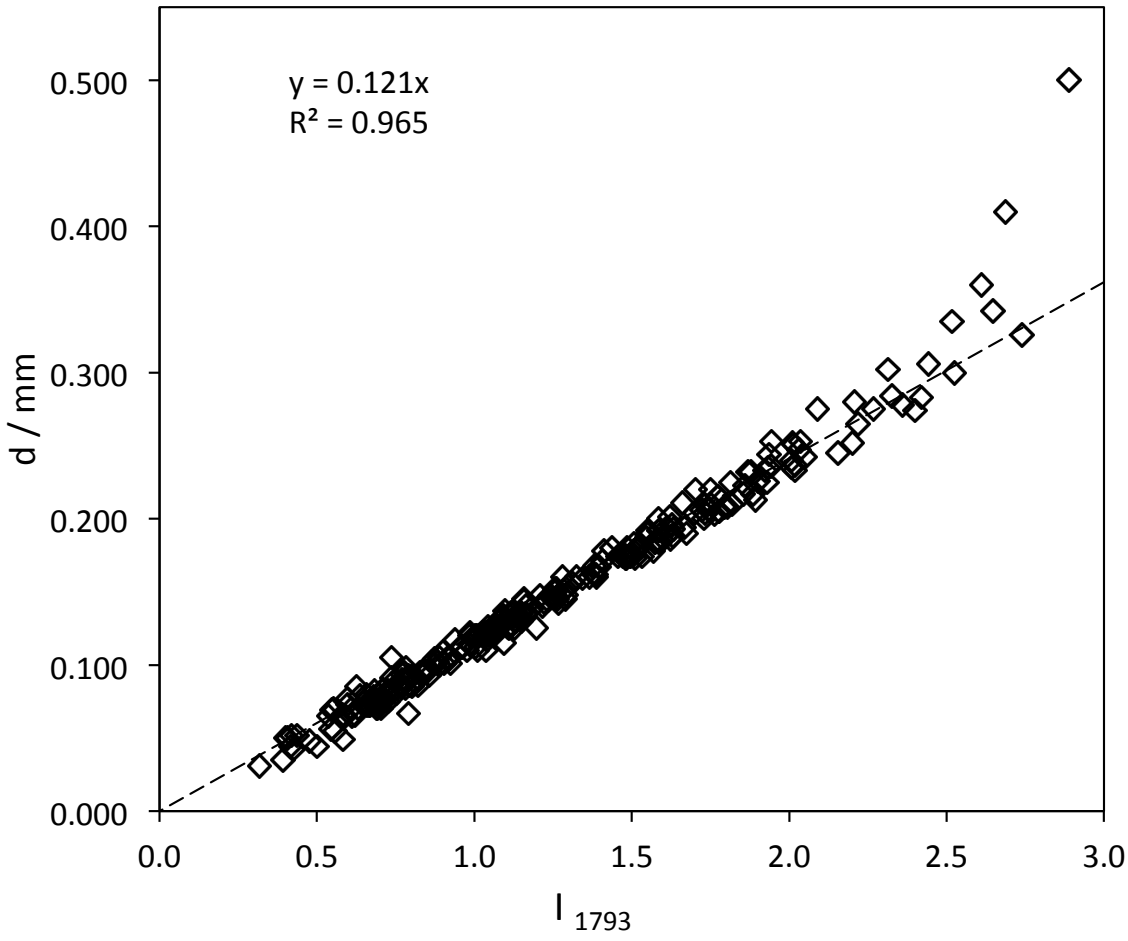
y = 0.121x
R² = 0.965
0.500
0.400
0.300
0.200
0.100
0.000
d / mm
0.0
0.5
1.0
1.5
2.0
2.5
3.0
I 1793

Figure 3b

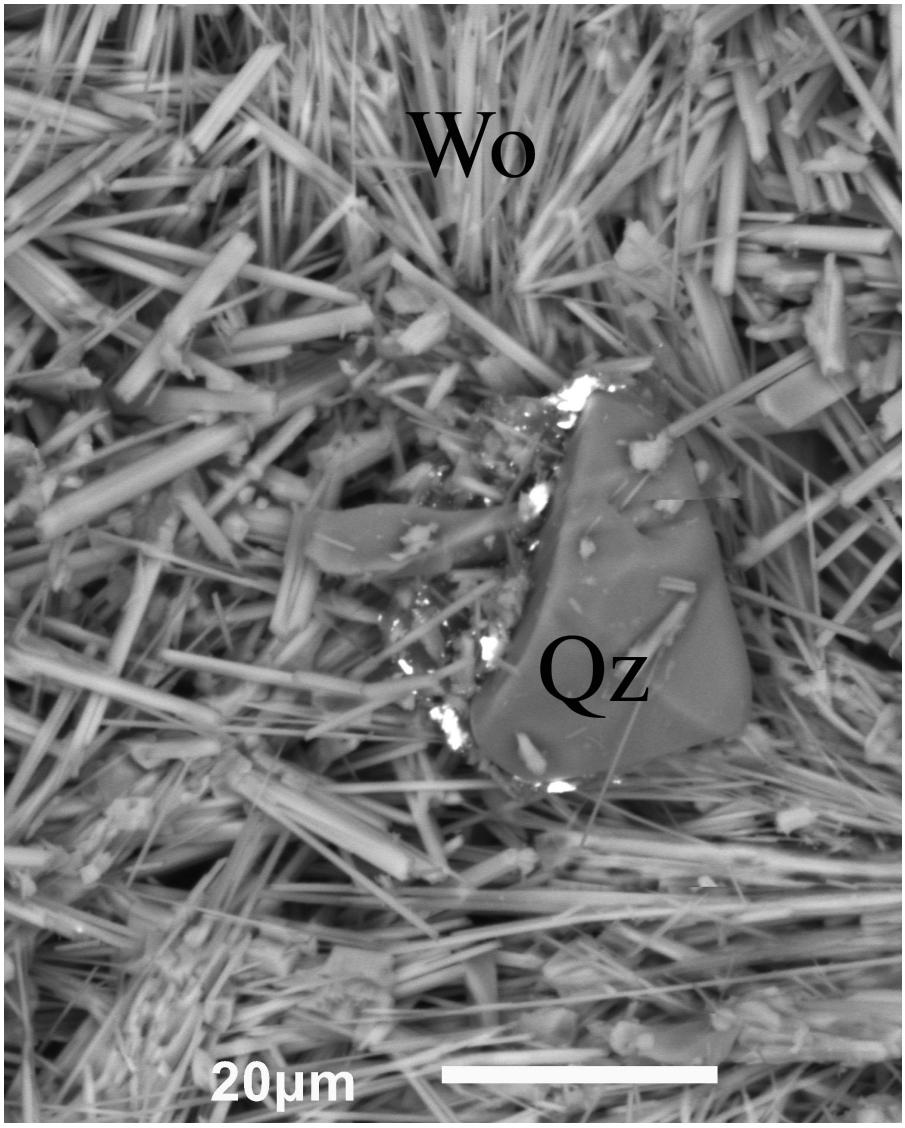

Figure 4

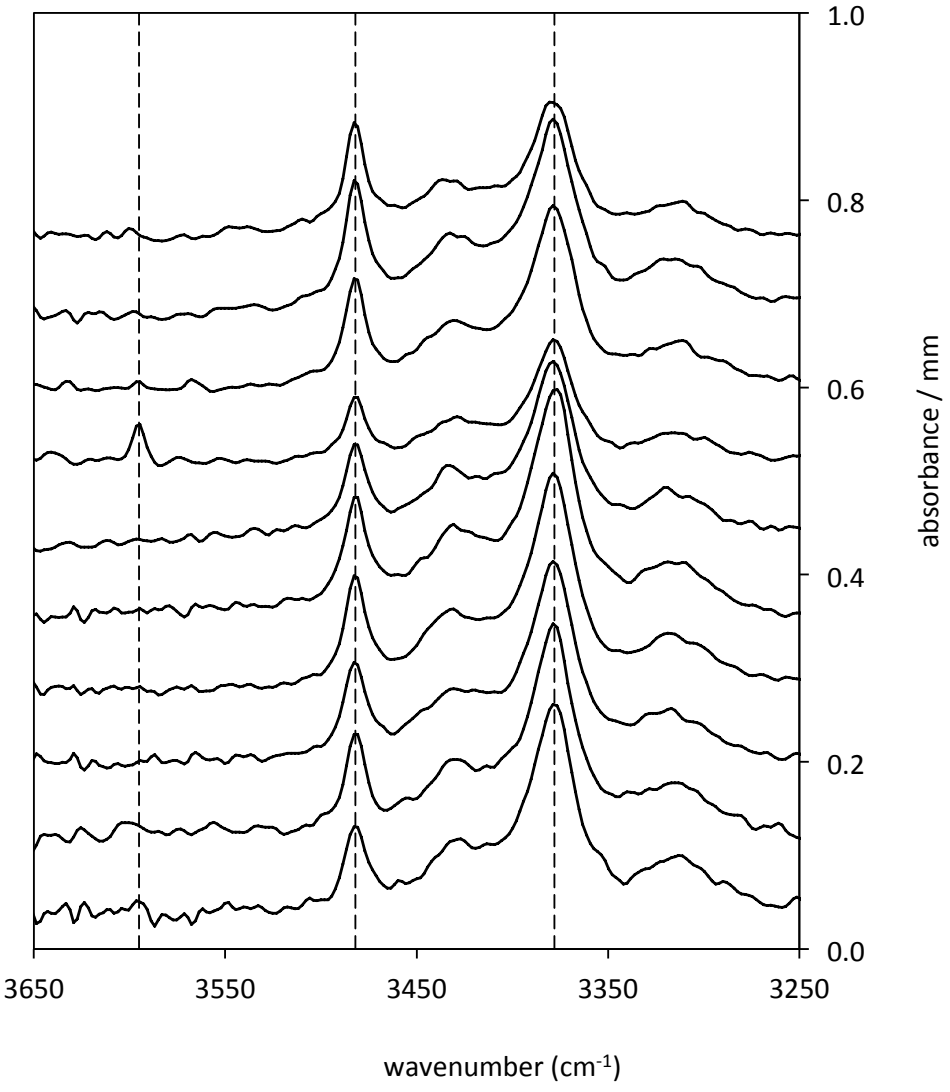
1.0
0.8
0.6
0.4
0.2
0.0
absorbance / mm
3650
3550
3450
3350
3250
wavenumber (cm-1)

Figure 5a

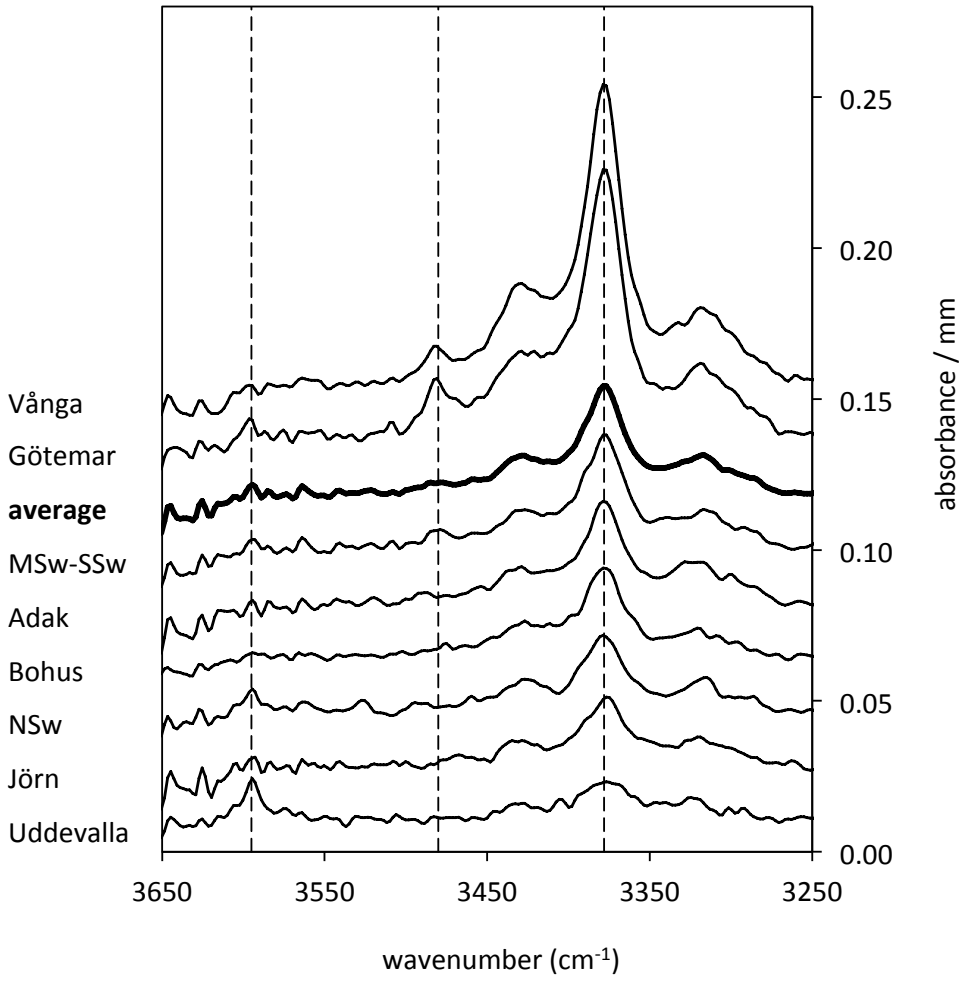
Vånga
Götemar
average
MSw-SSw
Adak
Bohus
NSw
Jörn
Uddevalla
0.25
0.20
0.15
0.10
0.05
0.00
absorbance / mm
3650
3550
3450
3350
3250
wavenumber (cm-1)

Figure 5b

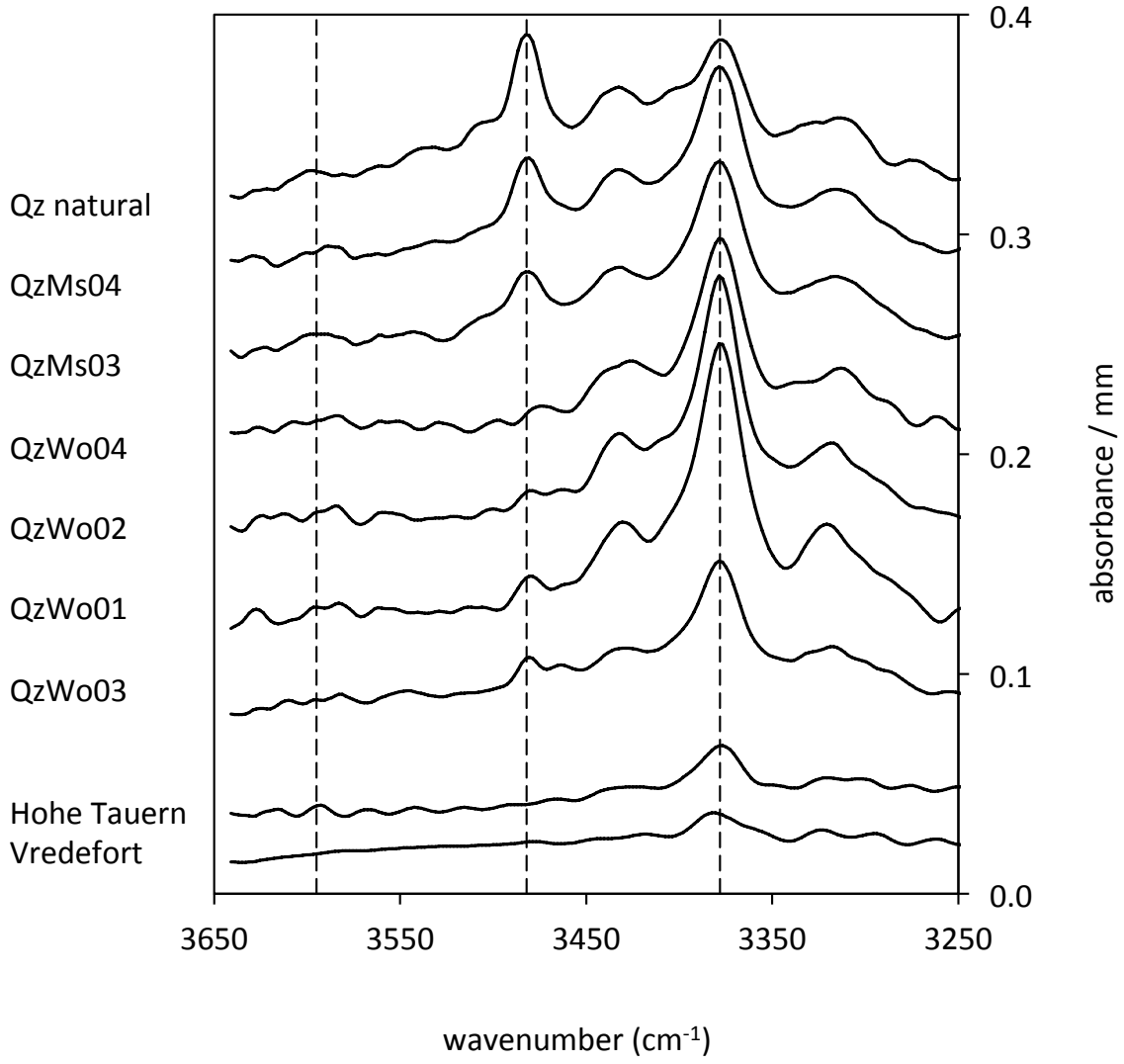
Qz natural
QzMs04
QzMs03
QzWo04
QzWo02
QzWo01
QzWo03
Hohe Tauern
Vredefort
0.4
0.3
0.2
0.1
0.0
absorbance / mm
3650
3550
3450
3350
3250
wavenumber (cm-1)

Figure 6

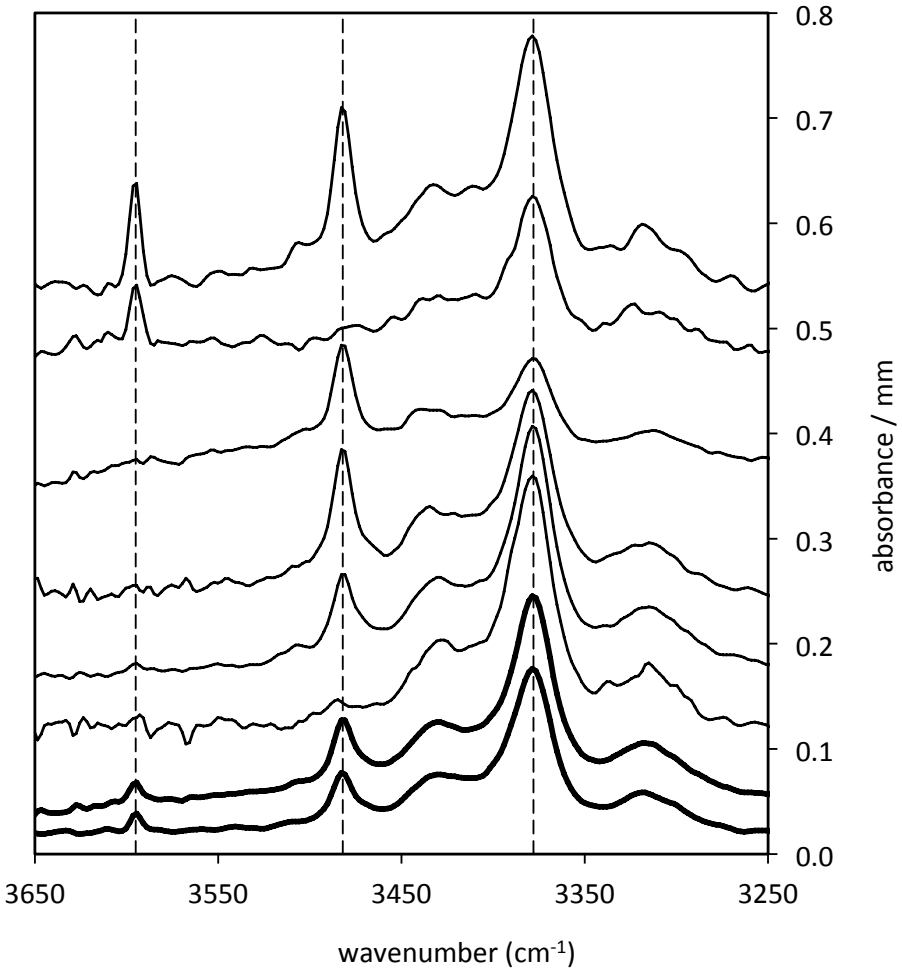
0.8
0.7
0.6
0.5
0.4
0.3
0.2
0.1
0.0
absorbance / mm
3650
3550
3450
3350
3250
wavenumber (cm-1)

Figure 7a

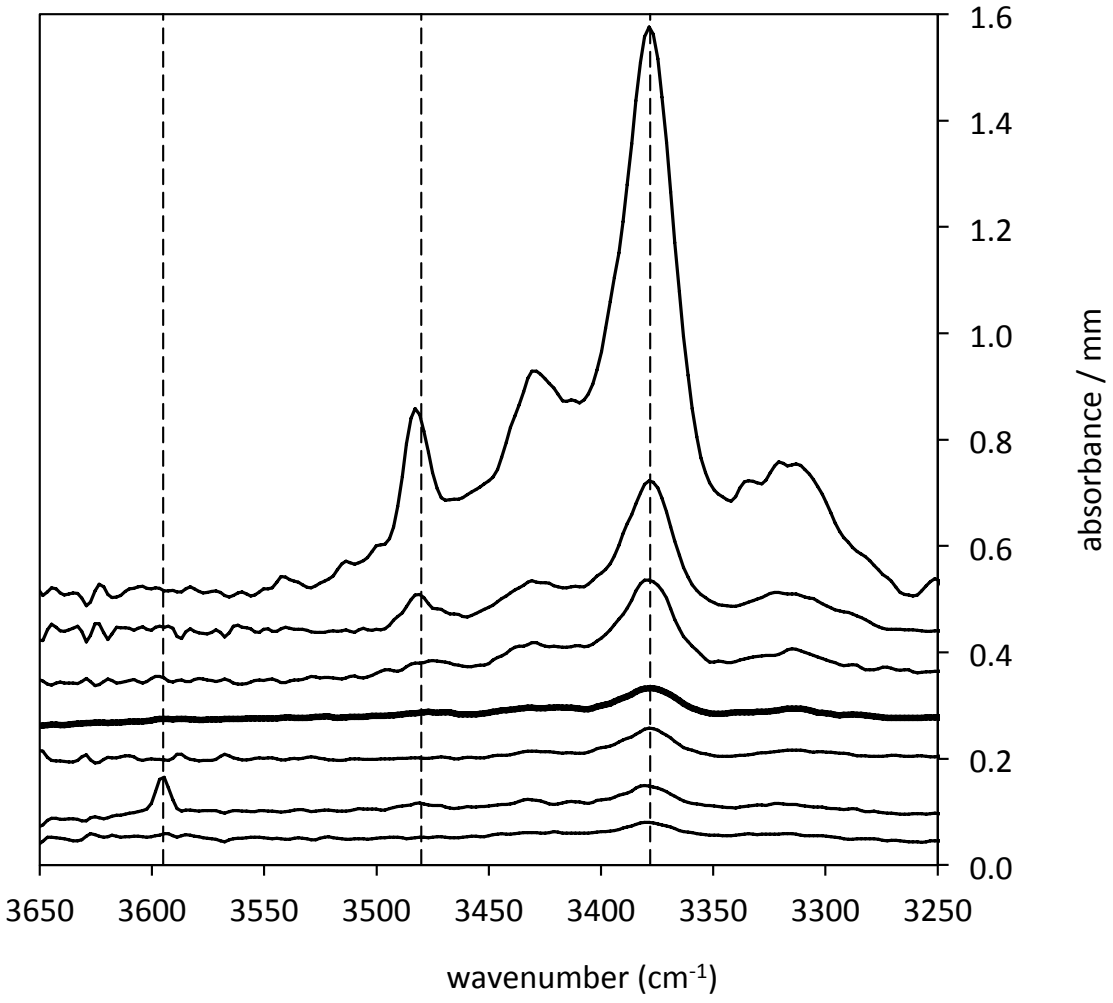
1.6
1.4
1.2
1.0
0.8
0.6
0.4
0.2
0.0
absorbance / mm
3650
3600
3550
3500
3450
3400
3350
3300
3250
wavenumber (cm-1)

Figure 7b

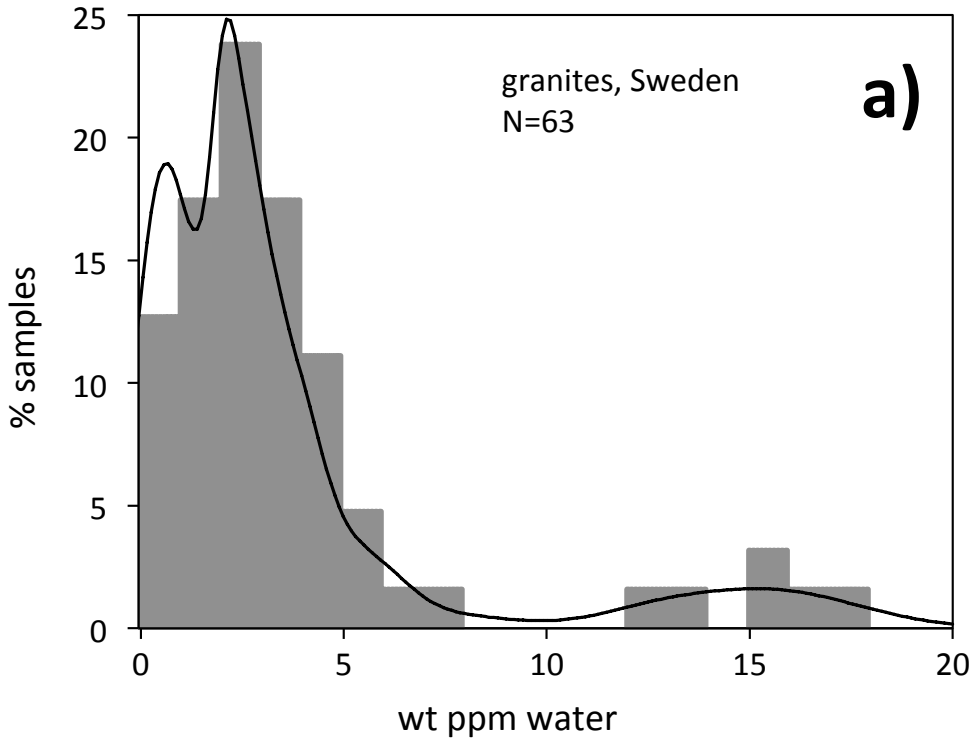

Figure 8a

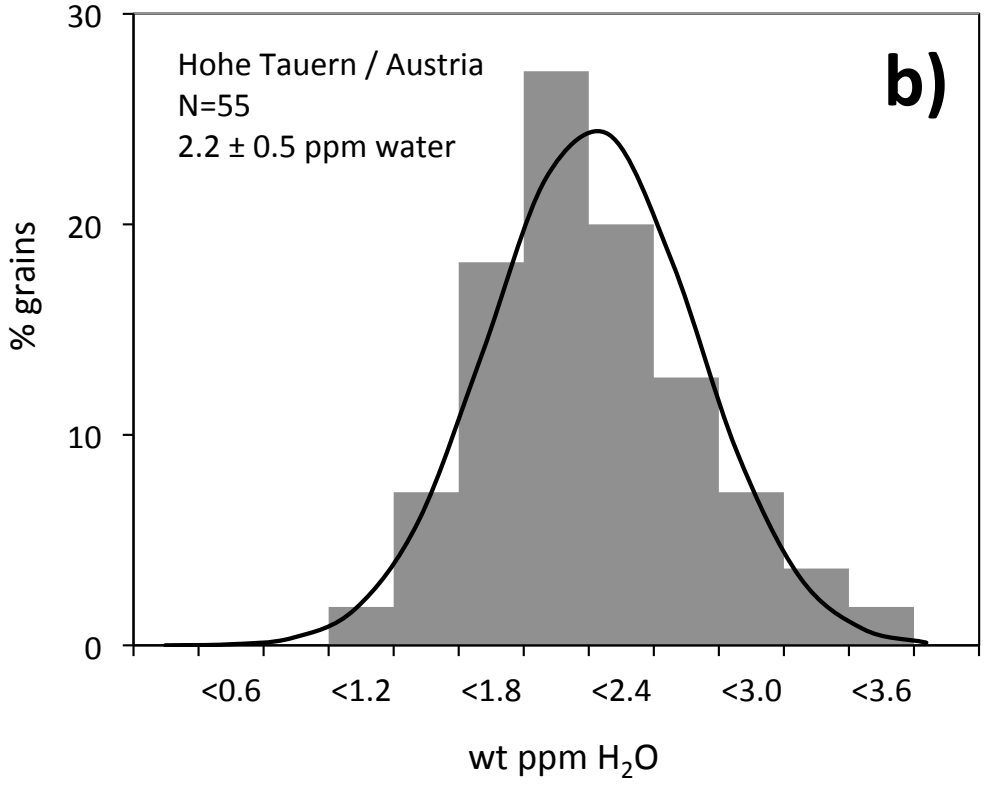
Hohe Tauern / Austria
N=55
2.2 ± 0.5 ppm water
b)
% grains
30
20
10
0
<0.6
<1.2
<1.8
<2.4
<3.0
<3.6
wt ppm H_2O

Figure 8b

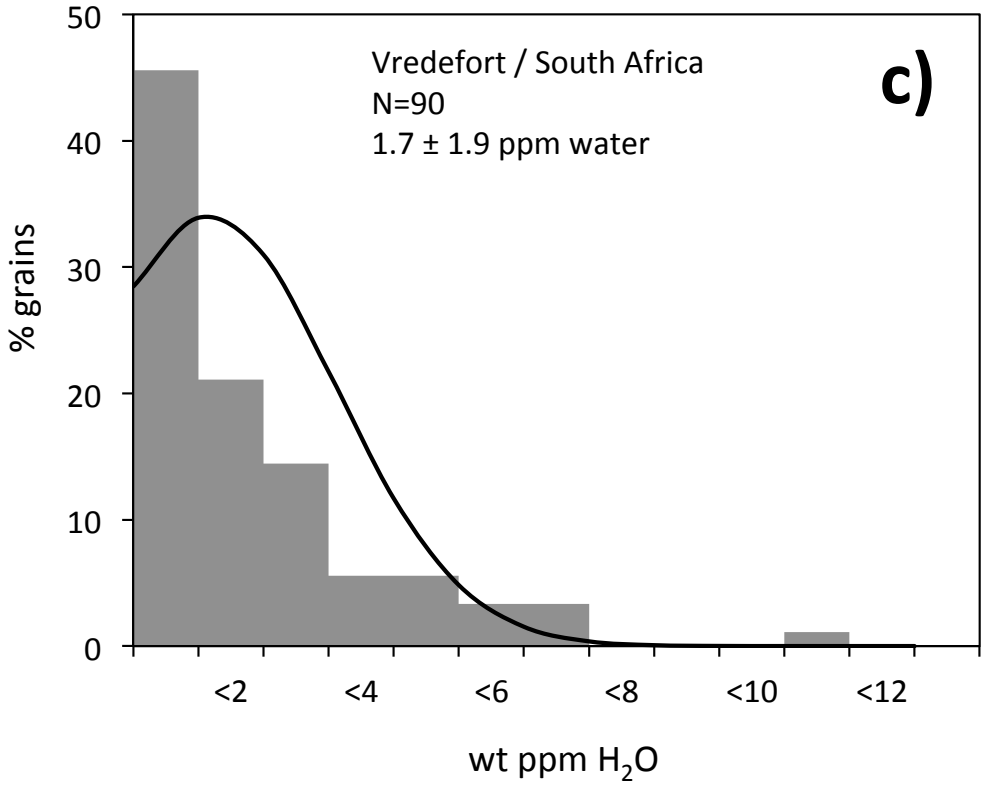
Vredefort / South Africa
N=90
1.7 ± 1.9 ppm water
c)
% grains
50
40
30
20
10
0
<2
<4
<6
<8
<10
<12
wt ppm H_2O

Figure 8c

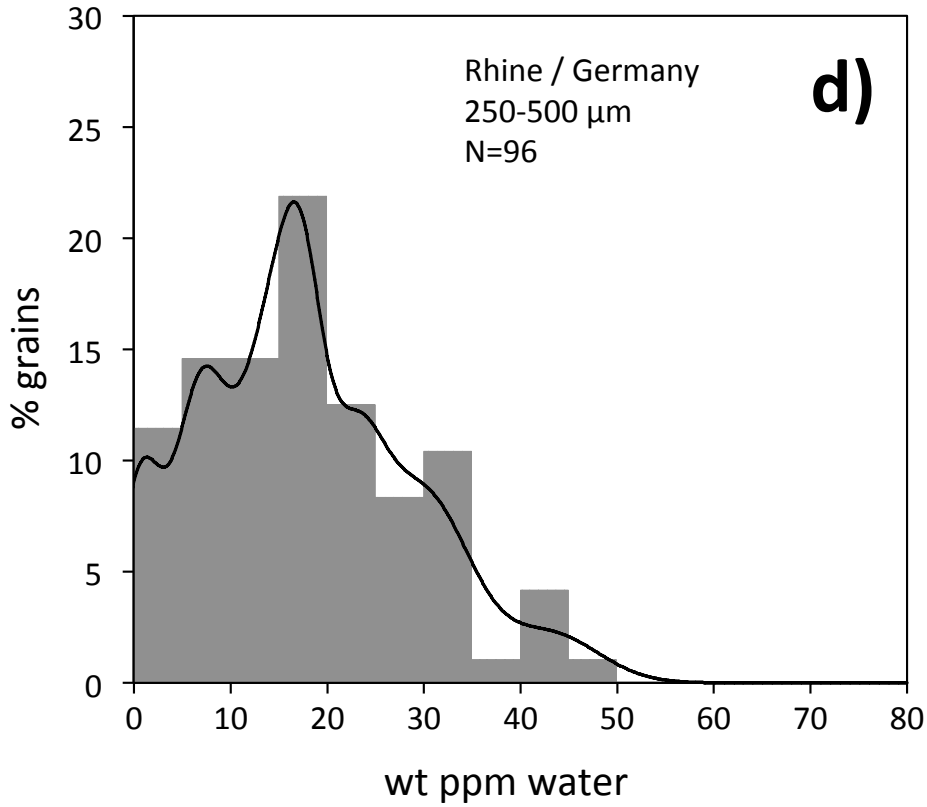
Rhine / Germany
250-500 µm
N=96
d)
% grains
wt ppm water
0
5
10
15
20
25
30
0
10
20
30
40
50
60
70
80

Figure 8c

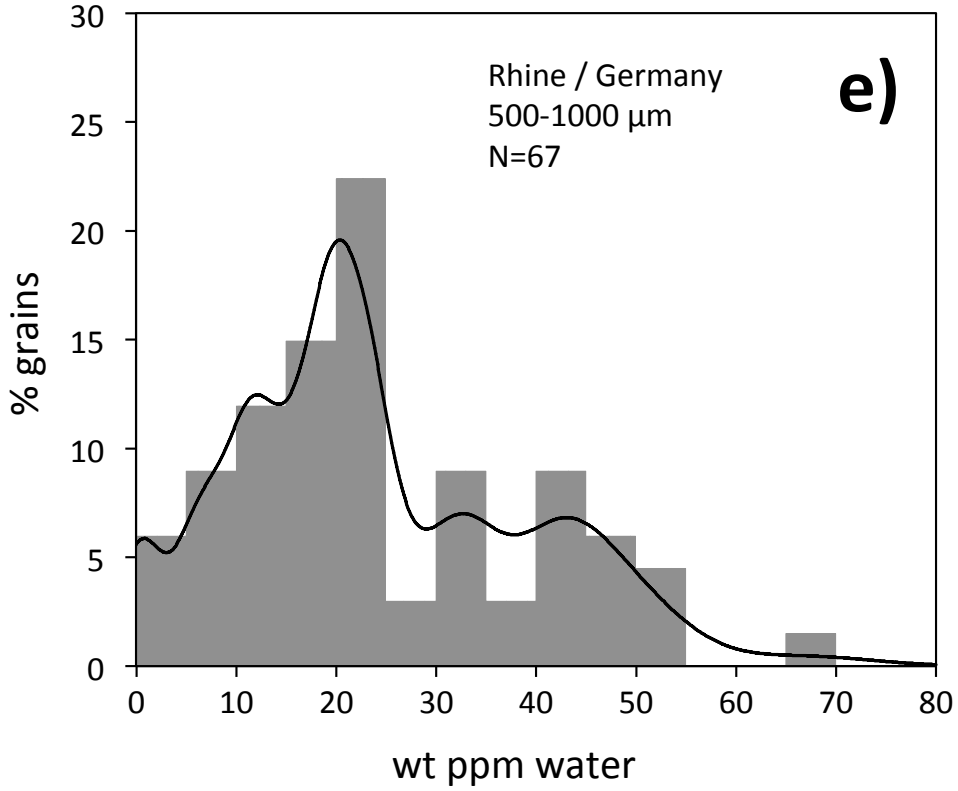
Rhine / Germany
500-1000 µm
N=67
e)
% grains
wt ppm water
0
5
10
15
20
25
30
0
10
20
30
40
50
60
70
80

Figure 8e

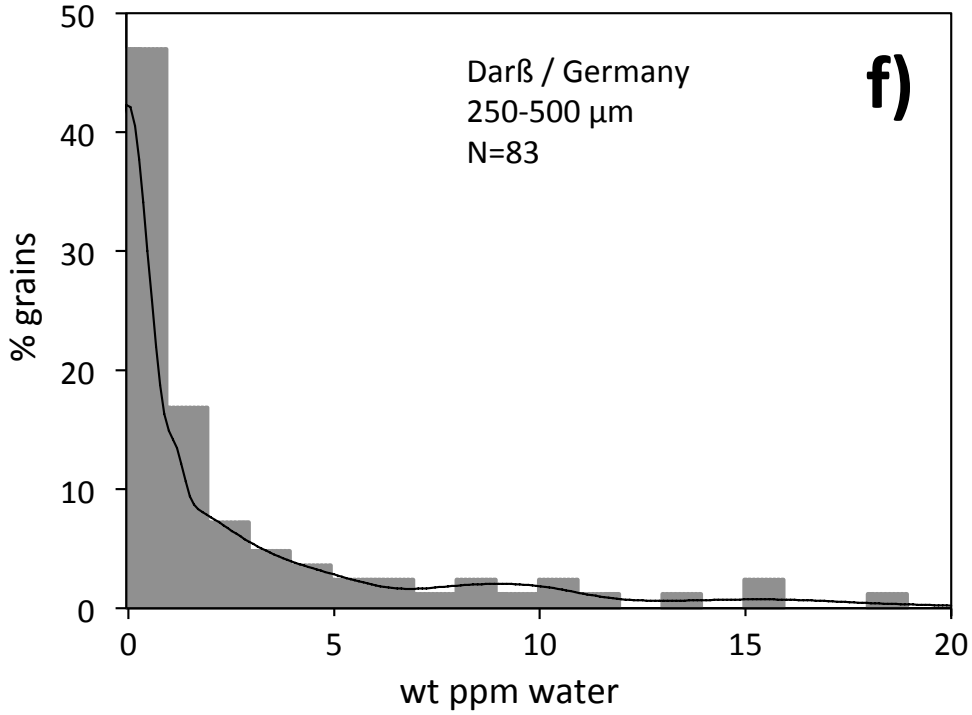
Darß / Germany
250-500 µm
N=83
f)
% grains
wt ppm water
0
10
20
30
40
50
0
5
10
15
20

Figure 8f

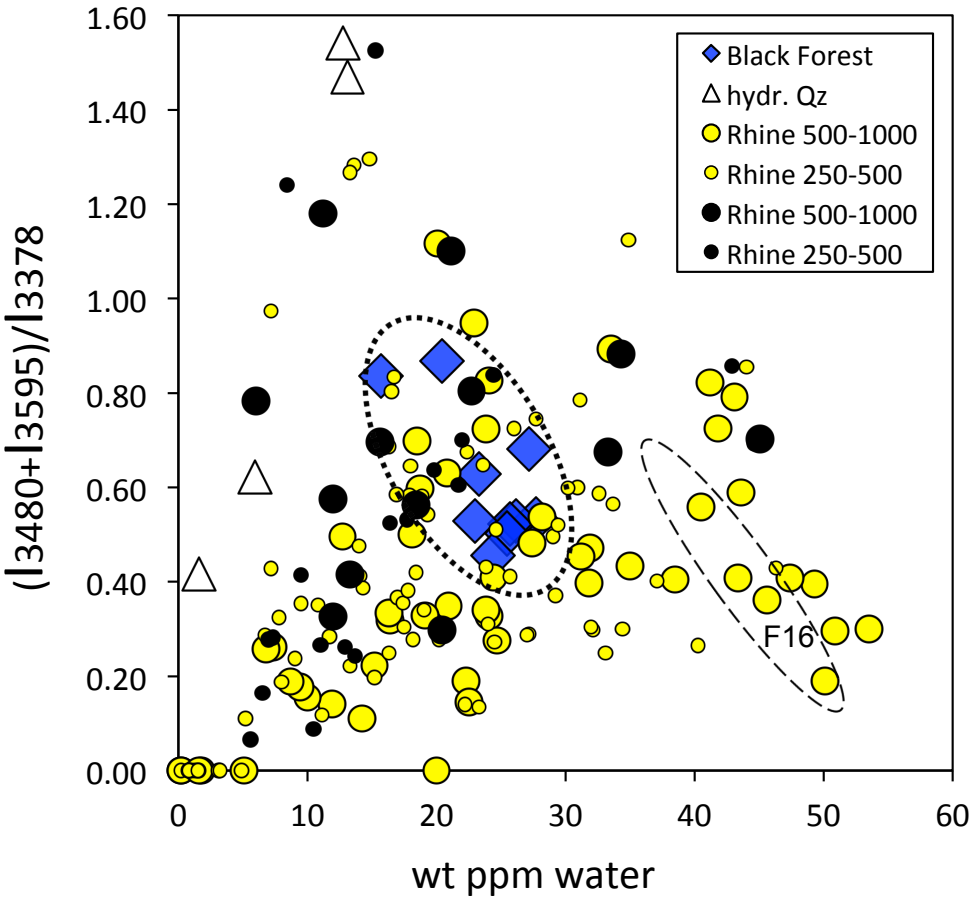
1.60
1.40
1.20
1.00
0.80
0.60
0.40
0.20
0.00
0
10
20
30
40
50
60
wt ppm water
(I3480+I3595)/I3378
Black Forest
hydr. Qz
Rhine 500-1000
Rhine 250-500
Rhine 500-1000
Rhine 250-500
F16

Figure 9

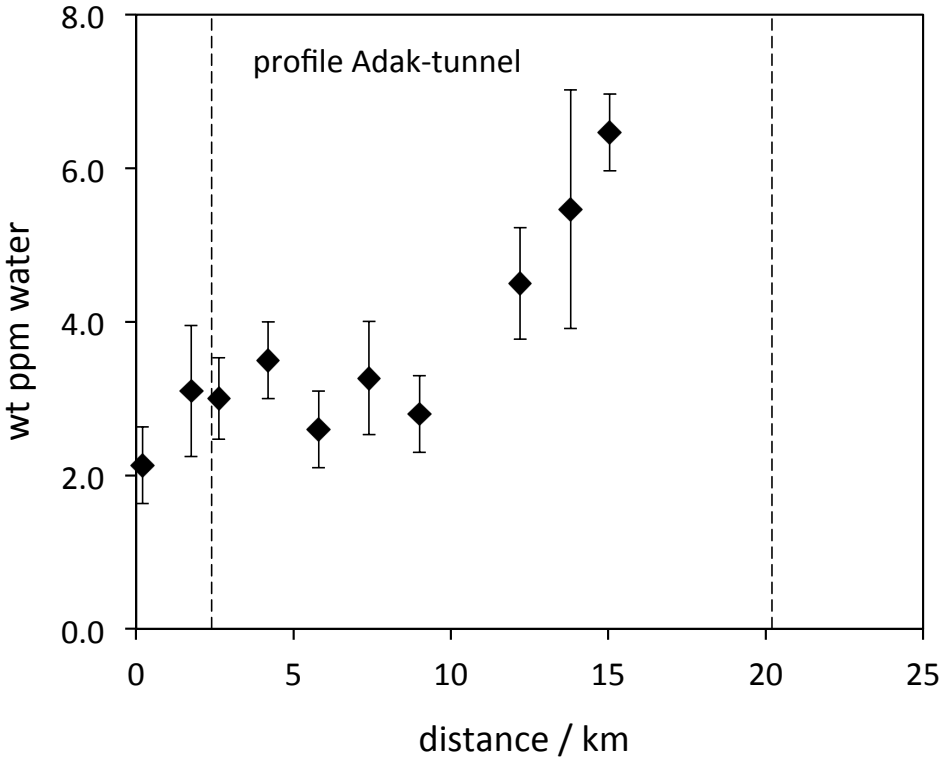
profile Adak-tunnel
wt ppm water
distance / km
8.0
6.0
4.0
2.0
0.0
0
5
10
15
20
25

Figure 10

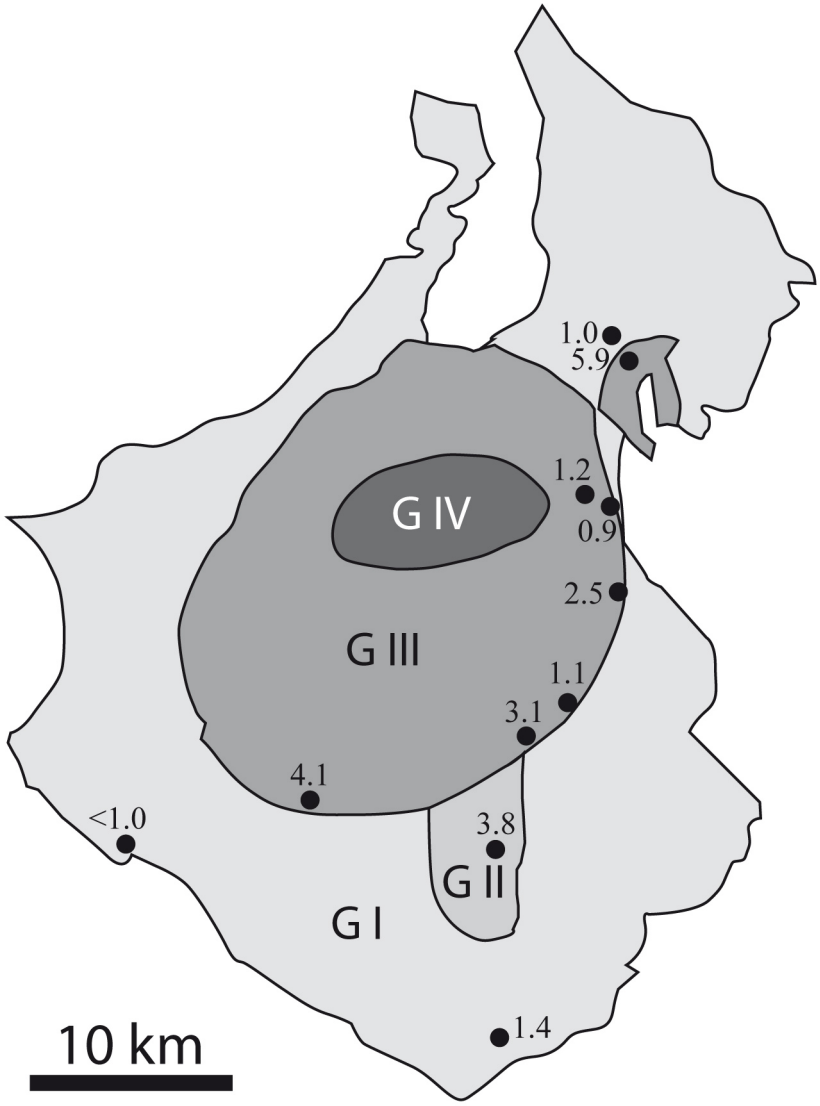

Figure 11

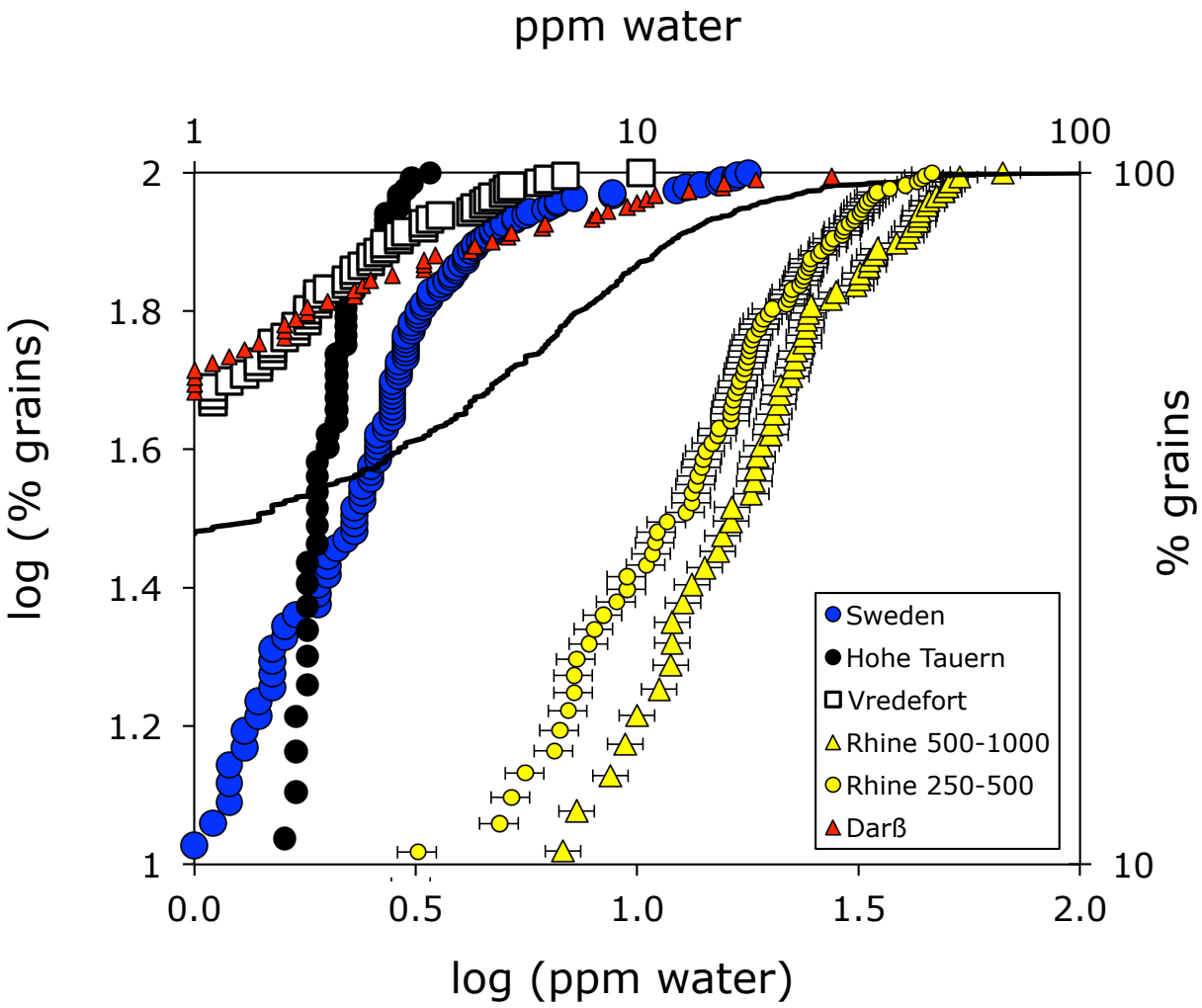
ppm water
1
10
100
2
1.8
1.6
1.4
1.2
1
100
10
log (% grains)
% grains
0.0
0.5
1.0
1.5
2.0
log (ppm water)
Sweden
Hohe Tauern
Vredefort
Rhine 500-1000
Rhine 250-500
Darß

Figure 12

Table 1: Sample descriptions and OH-contents

Sample number	Sample	Locality	Latitude	Longitude	N (crystals)
	Proterozoic granites from Sweden				
67015	granite	Lina granite	67.25 N	20.25 E	2
67014	granite	Lina granite	67.18 N	20.67 E	2
73294	granite	Degerberg granite	66.00 N	23.17 E	2
73188	granite	Degerberg granite	65.63 N	22.82 E	2
73195	granite	Åde granite	65.65 N	22.97 E	2
67029	granite	Sorsele granite	65.89 N	17.35 E	2
67028	granite	Sorsele granite	65.88 N	17.51 E	2
65163	granite	Arvidsjaur granite	65.66 N	20.23 E	2
65158	granite	Arvidsjaur granite	65.60 N	19.18 E	2
65165	granite	Arvidsjaur granite	65.54 N	20.48 E	2
72157	granite	Adak granite	65.40 N	18.68 E	3
72159	granite	Adak granite	65.40 N	18.71 E	3
72160	granite	Adak granite	65.39 N	18.72 E	3
72162	granite	Adak granite	65.39 N	18.75 E	3
72164	granite	Adak granite	65.38 N	18.78 E	3
72166	granite	Adak granite	65.37 N	18.81 E	3
72168	granite	Adak granite	65.37 N	18.84 E	3
72172	granite	Adak granite	65.36 N	18.90 E	4
72174	granite	Adak granite	65.35 N	18.93 E	3
72176	granite	Adak granite	65.34 N	18.96 E	3
65147	granite	Jörn granite	65.28 N	20.22 E	2
65148	granite	Jörn granite	65.26 N	20.25 E	2
65155	granite	Jörn granite	65.21 N	20.17 E	2
65154	granite	Jörn granite	65.21 N	20.20 E	2
65144	granite	Jörn granite	65.18 N	20.20 E	2
2002-006	granite	Jörn granite	65.14 N	20.12 E	3
65143	granite	Jörn granite	65.12 N	20.11 E	2
65157	granite	Jörn granite	65.10 N	19.85 E	2
2000-018	granite	Jörn granite	65.09 N	19.69 E	3
65142	granite	Jörn granite	65.09 N	20.08 E	2
65139	granite	Jörn granite	65.01 N	20.09 E	2
67047	granite	Revsund granite	65.30 N	17.66 E	2
67045	granite	Revsund granite	64.89 N	20.14 E	2
65114	granite	Rätan granite	61.80 N	14.68 E	2
65115	granite	Rätan granite	61.79 N	14.87 E	2
65108	granite	Dala granite	61.55 N	14.84 E	2

65109	granite	Dala granite	61.51 N	14.66 E	2
73175	granite	Filipstad granite	60.15 N	13.54 E	2
73176	granite	Filipstad granite	60.09 N	13.61 E	2
2000-020	granite	Dyke/Fogdösten	60.13 N	18.80 E	1
97037	granite	Early Svecofennian granit	59.34 N	18.27 E	2
72090	granite	Bohus granite	58.67 N	11.34 E	2
72087	granite	Bohus granite	58.30 N	11.53 E	2
70137	granite	Uddevalla granite	58.36 N	11.97 E	2
70141	granite	Uddevalla granite	58.35 N	12.04 E	2
74126	granite	Småland granite	57.58 N	16.51 E	2
72103	granite	Småland granite	57.57 N	16.70 E	2
72101	granite	Småland granite	57.54 N	16.71 E	2
74026	granite	Götemar granite	57.49 N	16.63 E	2
74027	granite	Götemar granite	57.49 N	16.63 E	2
74031	granite	Småland granite	57.02 N	15.00 E	2
72192	granite	Vånga granite	56.19 N	14.22 E	1
72189	granite	Vånga granite	56.18 N	14.35 E	1
72188	granite	Vånga granite	56.17 N	14.36 E	1
72187	granite	Vånga granite	56.17 N	14.36 E	1
72186	granite	Vånga granite	56.16 N	14.36 E	1
72190	granite	Vånga granite	56.16 N	14.38 E	1
72193	granite	Vånga granite	56.15 N	14.36 E	1
72185	granite	Vånga granite	56.13 N	14.37 E	1
	other samples				
	granite	Black Forest / Germany	48.59 N	8.21 E	10
	quartzite	Hohe Tauern / Austria	47.07 N	12.38 E	55
	quartzite	Vredefort / South Africa	26.88 S 26.85 S	27.23 E 27.64 E	90
	river sediment 250-500 µm	Rhöndorf / Germany	50.66 N	7.21 E	96
	river sediment 500-1000 µn	Rhöndorf / Germany	50.66 N	7.21 E	67
	beach sand	Darß / Germany	54.48 N	12.51 E	83

[1] calculated using calibration of Libowitzky and Rossman (1997); b.d.l. = below detection limit

Average OH content (wt ppm water) [1]	Range OH content (wt ppm water) [1]
2.8	2.5 - 3.0
3.0	2.9 - 3.1
1.5	1.0 - 2.0
4.1	3.7 - 4.5
4.8	3.9 - 5.7
2.8	2.6 - 3.0
2.7	2.5 - 2.8
3.7	3.1 - 4.3
1.0	0.5 - 1.4
2.4	2.0 - 2.8
2.1	1.7 - 2.4
3.1	2.3 - 4.0
3.0	2.4 - 3.4
3.5	3.3 - 3.8
2.6	2.1 - 2.9
3.3	2.7 - 4.1
2.8	2.7 - 2.9
4.5	3.6 - 5.3
5.5	4.2 - 7.2
6.5	6.2 - 6.6
1.0	0.8 - 1.2
5.9	3.0 - 8.8
1.2	0.9 - 1.5
0.9	0.9
2.5	2.3 - 2.6
1.1	0.9 - 1.2
3.1	2.5 - 3.6
4.1	2.8 - 5.3
b.d.l.	
3.8	3.4 - 4.1
1.4	1.2 - 1.5
4.3	4.1 - 4.4
0.8	0.5 - 1
3.3	3.2 - 3.3
4.7	4.6 - 4.7
2.3	1.6 - 3.0

17.4	16.9 - 17.8
2.1	2.0 - 2.2
1.9	1.9
1.6	
2.0	1.3 - 2.6
3.4	2.8 - 3.9
3.2	3.1 - 3.2
2.3	1.9 - 2.6
2.6	2.4 - 2.8
1.0	0.4 - 1.5
2.9	2.8 - 2.9
2.5	2.3 - 2.6
7.6	6.4 - 8.8
12.6	12.3 - 12.9
1.4	1.3 - 1.5
1.4	
4.7	
15.3	
16.6	
13.9	
15.5	
5.6	
3.8	

23.9	15.7 - 27.7
2.2	1.1 - 3.4
1.7	0 - 10.2
18.2	0 - 46
24.6	0 - 67
4.3	0 - 114

Table 2: run conditions CSPV experiments

	phase assemblage	x CO_2	p(kbar)	T(°C)	t (h)
QzMs03	Qz + Ms	0*	3	650	213
QzMs04	Qz + Ms	0*	3	650	78
QzWo01	Qz + Wo +CO_2	1	1	750	65
QzWo02	Qz + Wo +CO_2 + H_2O	0.13	1	750	70
QzWo03	Qz + Wo +CO_2	1	1	750	4
QzWo04	Qz + Wo +CO_2	1	1	750	792

Qz = quartz, Ms= muscovite, Wo = wollastonite.

* = nominally no fluid present